

VYSOKÉ UČENÍ TECHNICKÉ V BRNĚ

BRNO UNIVERSITY OF TECHNOLOGY



FAKULTA STROJNÍHO INŽENÝRSTVÍ
ÚSTAV FYZIKÁLNÍHO INŽENÝRSTVÍ

FACULTY OF MECHANICAL ENGINEERING
INSTITUTE OF PHYSICAL ENGINEERING

OSTWALD RIPENING – THEORETICAL DESCRIPTION AND SIMULATION.

OSTWALDOVO ZRÁNÍ – TEORETICKÝ POPIS A SIMULACE.

BAKALÁŘSKÁ PRÁCE

BACHELOR'S THESIS

AUTOR PRÁCE

AUTHOR

Bc. TOMÁŠ ČECHAL

VEDOUCÍ PRÁCE

SUPERVISOR

Ing. JAN ČECHAL, Ph.D.

BRNO 2008

Vysoké učení technické v Brně, Fakulta strojního inženýrství

Ústav fyzikálního inženýrství

Akademický rok: 2007/08

ZADÁNÍ BAKALÁŘSKÉ PRÁCE

student(ka): Čechal Tomáš, Bc.

který/která studuje v **bakalářském studijním programu**

obor: **Fyzikální inženýrství (3901R012)**

Ředitel ústavu Vám v souladu se zákonem č.111/1998 o vysokých školách a se Studijním a zkušebním řádem VUT v Brně určuje následující téma bakalářské práce:

Ostwaldovo zrání – teoretický popis a simulace.

v anglickém jazyce:

Ostwald ripening – theoretical description and simulation.

Stručná charakteristika problematiky úkolu:

Teoretická a experimentální práce, simulace výsledků.

Cíle bakalářské práce:

Teoreticky popište proces Ostwaldova zrání, proveďte počítačovou simulaci a výsledky srovnajte s experimentem.

Seznam odborné literatury:

- [1] H. Lüth: Surfaces and Interfaces of Solid Materials, Third ed., Springer-Verlag, Berlin 1997.
- [2] K. Oura, V. G. Lifshits, A. A. Saranin, A. V. Zotov, M. Katayama: Surface Science An Introduction, Springer-Verlag, Berlin 2003.

Vedoucí bakalářské práce: Ing. Jan Čechal, Ph.D.

Termín odevzdání bakalářské práce je stanoven časovým plánem akademického roku 2007/08.

V Brně, dne 16.5.2008



prof. RNDr. Tomáš Šikola, CSc.
Ředitel ústavu



doc. RNDr. Miroslav Doupovec, CSc.
Děkan fakulty

LICENČNÍ SMLOUVA

POSKYTOVANÁ K VÝKONU PRÁVA UŽÍT ŠKOLNÍ DÍLO

uzavřená mezi smluvními stranami:

1. Pan/paní

Jméno a příjmení: Bc. Tomáš Čechal
Bytem: Zmola 125/35, 69604, Svatobořice-Mistřín - Mistřín
Narozen/a (datum a místo): 5.9.1983, Kyjov

(dále jen "autor")

a

2. Vysoké učení technické v Brně

Fakulta strojního inženýrství
se sídlem Technická 2896/2, 61669 FSI VUT v Brně
jejímž jménem jedná na základě písemného pověření děkanem fakulty:

.....

(dále jen "nabyvatel")

Článek 1

Specifikace školního díla

1. Předmětem této smlouvy je vysokoškolská kvalifikační práce (VŠKP):

- disertační práce
- diplomová práce
- bakalářská práce

jiná práce, jejíž druh je specifikován jako

(dále jen VŠKP nebo dílo)

Název VŠKP: Ostwaldovo zrání – teoretický popis a simulace.

Vedoucí/školitel VŠKP: Ing. Jan Čechal, Ph.D.

Ústav: Ústav fyzikálního inženýrství

Datum obhajoby VŠKP:

VŠKP odevzdal autor nabyvateli v:

- tištěné formě - počet exemplářů
- elektronické formě - počet exemplářů

2. Autor prohlašuje, že vytvořil samostatnou vlastní tvůrčí činností dílo shora popsané a specifikované. Autor dále prohlašuje, že při zpracovávání díla se sám nedostal do rozporu s autorským zákonem a předpisy souvisejícími a že je dílo dílem původním.

3. Dílo je chráněno jako dílo dle autorského zákona v platném znění.

4. Autor potvrzuje, že listinná a elektronická verze díla je identická.

Článek 2
Udělení licenčního oprávnění

1. Autor touto smlouvou poskytuje nabyvateli oprávnění (licenci) k výkonu práva uvedené dílo nevýdělečně užít, archivovat a zpřístupnit ke studijním, výukovým a výzkumným účelům včetně pořizování výpisů, opisů a rozmnoženin.
2. Licence je poskytována celosvětově, pro celou dobu trvání autorských a majetkových práv k dílu.
3. Autor souhlasí se zveřejněním díla v databázi přístupné v mezinárodní síti
 - ihned po uzavření této smlouvy
 - 1 rok po uzavření této smlouvy
 - 3 roky po uzavření této smlouvy
 - 5 let po uzavření této smlouvy
 - 10 let po uzavření této smlouvy(z důvodu utajení v něm obsažených informací)
4. Nevýdělečné zveřejňování díla nabyvatelem v souladu s ustanovením § 47b zákona č. 111/1998 Sb., v platném znění, nevyžaduje licenci a nabyvatel je k němu povinen a oprávněn ze zákona.

Článek 3
Závěrečná ustanovení

1. Smlouva je sepsána ve třech vyhotoveních s platností originálu, přičemž po jednom vyhotovení obdrží autor a nabyvatel, další vyhotovení je vloženo do VŠKP.
2. Vztahy mezi smluvními stranami vzniklé a neupravené touto smlouvou se řídí autorským zákonem, občanským zákoníkem, vysokoškolským zákonem, zákonem o archivnictví, v platném znění a popř. dalšími právními předpisy.
3. Licenční smlouva byla uzavřena na základě svobodné a pravé vůle smluvních stran, s plným porozuměním jejímu textu i důsledkům, nikoliv v tísní a za nápadně nevýhodných podmínek.
4. Licenční smlouva nabývá platnosti a účinnosti dnem jejího podpisu oběma smluvními stranami.

V Brně dne:

.....

Nabyvatel

.....

Autor

Anotace

Tato práce se zabývá popisem Ostwaldova zrání trojrozměrných ostrůvků deponovaných na rovinných površích. V první kapitole jsou představeny dvě teorie Ostwaldova zrání: LSW teorie založená na aproximaci středního pole a mnohačasticová teorie vycházející z řešení difuzní rovnice v kvazistatické aproximaci. Ve druhé kapitole je popsán algoritmus numerického řešení rovnic získaných z mnohačasticové teorie. Výsledky numerického řešení jsou ve třetí kapitole srovnány s předpověďmi LSW modelu.

Bylo zjištěno, že předpovědi standardní LSW teorie popisující systémy s dvourozměrným transportem hmoty jsou v ostrém protikladu jak s výsledky získanými z dokonalejšího mnohačasticového modelu, tak s experimenty popsány v uvedených pramenech. Mnohačasticový model založený na difuzní rovnici poskytuje výsledky konzistentní s jinými teoriemi i experimentem.

Abstract

This thesis deals with Ostwald ripening of three-dimensional clusters deposited on a two-dimensional surface. In the first chapter two distinct theories of Ostwald ripening are presented: the mean-field LSW theory and a many-body theory based on the solution of the diffusion equation in quasistationary approximation. In the second chapter the algorithm used for numerical solution of the equations obtained from the many-body theory is described. The results extracted from the numerical solution are compared with predictions of the LSW model in the third chapter.

We found that the standard LSW theory of systems with two-dimensional mass transport should not be used in practice because its predictions are in strong disagreement with the results obtained both from the more elaborate diffusion-equation model and from experimental studies described in references. On the other hand, the diffusion-equation based model gives results consistent with other theories and experiments.

Klíčová slova: fázová separace, Ostwaldovo zrání, LSW teorie, numerická simulace
Keywords: phase separation, Ostwald ripening, LSW theory, numeric simulation

ČECHAL, T. Ostwaldovo zrání – teoretický popis a simulace. Brno: Vysoké učení technické v Brně, Fakulta strojního inženýrství, 2008. 46 s. Vedoucí bakalářské práce Ing. Jan Čechal, Ph.D.

Prohlašuji, že jsem na této bakalářské práci pracoval samostatně a použil jsem pouze pramenů uvedených v seznamu použité literatury.

V Brně dne 21. května 2008

Na tomto místě bych chtěl poděkovat vedoucímu práce Ing. Janu Čechalovi, Ph.D. za čas, který strávil podrobným pročítáním rukopisu a za cenné připomínky a rady, které pomohly zkvalitnit obsah této práce. Chtěl bych rovněž poděkovat Ing. Miroslavu Kolíbalovi za poskytnutí experimentálních dat a za podnětné diskuse, které mi pomohly k hlubšímu pochopení tématu. Zvláštní poděkování si zaslouží moji rodiče, bez jejichž podpory a zázemí, které vytvořili, by tato práce nemohla vzniknout.

Contents

1	The theory of Ostwald ripening	3
1.1	Mean-field and many-body theories	3
1.2	Possible approaches to the problem	4
1.3	Basic quantities related to ripening systems	6
1.4	The LSW theory	7
1.4.1	The growth rate equation	8
1.4.2	Mean island radius	9
1.4.3	Conservation of mass	10
1.4.4	The equation of continuity	10
1.5	A many-body theory for 3D/2D systems	11
1.5.1	Basic equations for the numerical simulation	11
1.5.2	Solution of the diffusion equation	13
1.5.3	The Ewald summation technique	14
1.5.4	Scaling properties of simulation equations	16
1.5.5	Matrix form of the simulation equations	17
2	The simulation algorithm	19
2.1	The initial set of islands	19
2.1.1	Initial distribution of island sizes	19
2.1.2	Initial island positions	20
2.1.3	The asymptotic behavior of the system	21
2.2	The initialization part	21
2.3	Finding the growth rates	22
2.4	Updating the island radii	23
2.5	Removing islands from the system	23
2.6	Implementation	23
2.7	Possible improvements of the algorithm	24
3	Results	25
3.1	Mean island radius	25
3.2	Shape histograms	32
3.3	Spatial histograms	34
3.4	Radial distribution functions	37

Introduction

A series of experiments studying the self-limited Ostwald ripening of gallium nanoclusters on silicon surfaces was performed at the Department of Solid State Physics and Surfaces of Institute of Physical Engineering at Faculty of Mechanical Engineering, Brno University of Technology, in fall and winter 2007. A theory describing the process of self-limited growth exists; however, it is a mean-field theory which ignores cluster-cluster interactions. Our experiments were performed at very high areal coverages and we therefore expect the cluster-cluster interaction to play an important role. The need therefore appeared of a more precise treatment which would take these interaction into account. Since the problem considered is far too difficult to be solved analytically we decided to perform a numerical simulation.

The purpose of this work is to compare the simplest possible mean-field model, the LSW theory, with a much more sophisticated approach based on the solution of the steady-state diffusion equation. These models will be used to predict the results of a simplified version of our real experiment. With a comparison of these results in hand, we should be able to appreciate the importance of cluster-cluster interactions and decide whether a mean-field theory is sufficient to describe the ripening process or if a better model has to be used.

Chapter 1

The theory of Ostwald ripening

Suppose that a thin adsorbate layer is being deposited on a clean substrate surface. In the Volmer-Weber growth mode, the adsorbate atoms are more strongly bound to each other than to the substrate atoms and three-dimensional islands start to nucleate and grow right on the substrate [1]. Similar situation is observed in the Stranski-Krastanov growth mode, where the islands grow on a wetting layer formed by the adsorbate atoms.

The process of increasing the mean island size at the expense of decreasing the number of islands is referred to as *coarsening* [1]. Two main mechanisms of coarsening are distinguished: *coarsening by coalescence*, either static or dynamic, during which two smaller islands merge upon contact to form one larger island, and *ripening*, or more usually *Ostwald ripening*¹, during which larger islands grow and smaller ones shrink due to the adatom diffusion.

Coarsening by coalescence is crucial if the islands are mobile enough (dynamic coalescence in the early-stage coarsening) or in mass non-conserved systems with continuous deposition (static coalescence of large immobile islands). Ostwald ripening is the dominant coarsening mechanism during late-stage coarsening of mass-conserved systems.

1.1 Mean-field and many-body theories

The coarsening theories can be roughly divided into two following categories:

- *Mean-field theories* neglect the effect of island-island interactions (namely, diffusion interactions or interactions mediated by elastic deformation of substrate underlying the islands). These theories are relatively simple and are sufficient to predict the correct power-law time dependence of mean island volume and the existence of scale-invariant island size distribution, but they fail to predict the correct form of this distribution. Furthermore, they cannot, by their very nature, predict the spatial correlations of the island positions. However, mean-field theories are a good starting point to any serious analysis.

¹After Wilhelm Ostwald, who in 1896 first observed ripening of precipitates in three-dimensional matrix.

- *Many-body theories* are capable to take the island-island interaction into account. Although some of the predictions, e.g., the time evolution of the mean island volume, are approximately the same as in the case of mean-field theories, more sophisticated results (island size distribution function) are usually significantly altered by the interactions. Many-body theories are, except to trivial cases of no practical importance, impossible to solve analytically and only numerical solutions are available.

1.2 Possible approaches to the problem

In this thesis we will focus on describing the Ostwald ripening of a mixed 3D/2D system (3D islands on 2D substrate). There are three most widely used approaches to describe the coarsening of such a system: Monte Carlo simulations, rate equation models and models based on the solution of the diffusion equation.

- *Monte Carlo simulation.* The system consists of a substrate layer which forms a 2D array of lattice sites and a set of atoms which can occupy these sites. These atoms can jump from their current location to any adjacent unoccupied lattice site with probability proportional to $\exp(-E_B/kT)$, where E_B is the energy barrier for the jump. The Monte Carlo techniques are very powerful, since there are no restrictions on the areal coverage, deposition flux or the shape of the islands and they are not limited to the case of Ostwald ripening, but can be at the same time used to model nucleation and early stages of nucleation and coarsening by coalescence [2]. There are two main drawbacks of these methods: first, they are very time-consuming; various ways were developed to overcome this problem, such as the *accelerated* Monte Carlo simulation [3]. Second, there is no easy way to determine the size of the energy barriers E_B .
- *Rate equation approach.* The system is described in terms of the quantities $N_j(t)$, $j = 1, 2, \dots$ where $N_j(t)$ is the number of islands consisting of exactly j atoms at the time t . The evolution of the system is governed by a set of coupled, first-order ordinary differential equations (rate equations) of the form [4]

$$\frac{dN_j(t)}{dt} = n \left[\sigma_{j-1}^i N_{j-1}(t) - \sigma_j^i N_j(t) \right] + \left[\sigma_{j+1}^o N_{j+1}(t) - \sigma_j^o N_j(t) \right], \quad j > 1, \quad (1.1)$$

where σ_j^i is the capture cross-section and σ_j^o is the release cross-section of adatoms for an island having j atoms and n is the adatom concentration. The first problem with this approach is that there is no simple way to determine the form of the rate constants σ . This is very serious, since these constants contain all the information concerning the nature of the system (especially the dominant interactions and growth-limiting processes). Second, the number of equations needed to describe the late-stage coarsening when the islands contain many atoms can be very large. Hopefully, there are means to deal with this problem, such as solving the rate equations only for clusters of certain size j and interpolating between these selected values of j or letting the number of atoms in an island become a continuous variable and transforming the set of rate equations into one partial differential equation [5].

Furthermore, the rate equation model is basically a mean-field approach, since the rate constants usually do not depend on the positions of the islands, although there is no principal restriction concerning this. The advantages of this approach are: (i) nucleation and coalescence can be easily studied within the same framework, (ii) nonzero deposition flux can be easily included and (iii) the famous LSW mean-field model (see below) based on the diffusion equation can be recovered under certain assumptions [5].

- *Diffusion equation approach.* The system is treated as being composed of two distinct parts: a set of islands of defined size and shape and a background gas of adatoms. The evolution of the adatom concentration field $n(\mathbf{r}, t)$ is governed by the time-dependent diffusion equation

$$\frac{\partial n(\mathbf{r}, t)}{\partial t} = \mathcal{D}\Delta n(\mathbf{r}, t), \quad (1.2)$$

where \mathcal{D} is the adatom diffusivity, while the time evolution of the islands is given by the growth equation

$$\frac{dV}{dt} = 2\pi v_M J, \quad (1.3)$$

where V is the island volume, v_M is the molar volume of the adatom phase and J is the total adatom diffusion flux into the island (see below for the derivation). These equations are coupled by the boundary conditions for the adatom concentration field prescribed on the surface of each island. It is customary to use the steady-state approximation in which the time derivative on the left-hand side of (1.2) is neglected in order to simplify the situation. This simplification works well in three dimensions, but in two-dimensional systems a serious problem arises since the steady-state solution of diffusion equation has a logarithmic divergence for large r . This divergence can be treated in two ways: (i) if the system is mass-conserved, i.e., there is no deposition flux, the logarithmic terms exactly cancel each other and the divergence is resolved; (ii) one can define a *screening length* [4] to cut-off the diverging concentration field. The latter treatment suffers from the fact that the screening length is an artificial addition to the theory and therefore the degree of approximation cannot be estimated [4]. One of the main advantages of the diffusion equation approach is that it can be used to examine the spatial correlations in the system, i.e., it is a many-body approach. Furthermore, one can work with very large areal coverages (up to 40 %) and with islands of varying shapes [6]. Further extensions allowing for more general experimental conditions (e.g., systems where elastic interactions play an important role) also seem to be possible.

In this thesis we use two models based on the diffusion equation approach: the mean-field LSW model and a slightly improved version of the many-body model described in Yao *et al.* [7].

1.3 Basic quantities related to ripening systems

There are several quantities used to describe the state of a ripening system:

- Number of islands $N(t)$ present in the system at the time t , or, equivalently, the island number density $\mathcal{N}(t) = N(t)/L^2$, where L is the length of the side of the sample, which is assumed to be square.

- The mean island radius

$$\langle \rho(t) \rangle = \frac{1}{N(t)} \sum_{i=1}^N \rho_i(t), \quad (1.4)$$

where ρ_i is the radius of the i th island, and the mean island volume

$$\langle V(t) \rangle = \frac{1}{N(t)} \sum_{i=1}^N V_i(t), \quad (1.5)$$

where V_i is the volume of i th island. A power-law time dependence of $\langle \rho \rangle$ and $\langle V \rangle$ has been observed experimentally in most 3D/3D and 2D/2D systems; recent experiments suggest that the power-law scaling might apply also in 3D/2D systems.

- The island size distribution function $\phi(\rho, t)$, where $\phi(\rho, t) d\rho dt$ gives the probability of finding an island of radius $(\rho; \rho + d\rho)$ in the time interval $(t; t + dt)$. For 3D/3D and 2D/2D systems it is predicted that this distribution function is *scale-invariant* for t large enough: when the island size distribution is scaled by the time-dependent mean island radius, it assumes a unique time-independent form [8]. According to [9], the distribution function is self-similar if

$$\phi(\rho, t) = \phi \left\{ \left[\frac{\langle \rho(\lambda t) \rangle}{\langle \rho(t) \rangle} \right] \rho, \lambda t \right\} \quad (1.6)$$

holds for any λ from a certain interval.

- The mean nearest-neighbor distance

$$\langle r(t) \rangle = \frac{1}{N(t)} \sum_{i=1}^N |\mathbf{R}_i - \mathbf{R}_{i,n}| \quad (1.7)$$

where \mathbf{R}_i is the position of the i th island and $\mathbf{R}_{i,n}$ is the position of the nearest neighbor of the i th island.

- The nearest-neighbor distance distribution function $\psi(r, t)$, where $\psi(r, t) dr dt$ gives the probability of finding two islands separated by a distance between r and $r + dr$ in the time interval $(t; t + dt)$. This distribution was again found to be self-similar with mean nearest-neighbor distance being the time-dependent scaling factor [9].

- The individual radial distribution function $\xi_i(r, t)$ for i th island, where $\xi_i(r, t) dr$ is the ratio of the number of particles found in a circular shell of radius r and thickness dr around i th island to the expected number of particles in the same shell calculated from the mean particle number density:

$$\xi_i(r, t) = \frac{1}{N_r} \int_r^{r+dr} \sum_{j \neq i}^N \delta(|\mathbf{R}_i - \mathbf{R}_j|) dr, \quad N_r = 2\pi\mathcal{N}(t) \int_r^{r+dr} r dr. \quad (1.8)$$

The overall radial distribution function $\xi(r, t)$ is the average of the individual distribution functions $\xi_i(r, t)$,

$$\xi(r, t) = \frac{1}{N} \sum_{i=1}^N \xi_i(r, t). \quad (1.9)$$

Several experiments show the presence of a *denuded zone* around the islands. By this we mean that around every island there is a circular shell of a certain radius in which no other islands are present. The existence of this zone can be easily proven by means of the radial distribution function: it corresponds to the interval of r where $\xi(r, t)$ is appreciably lesser than unity.

1.4 The LSW theory

The first complete theory of Ostwald ripening, the famous LSW theory, was developed by Lifshitz and Slyozov [10] and by Wagner [11]. The original LSW theory considered only the case of three-dimensional particles deposited in three-dimensional matrix; later it was extended by Chakraverty² to the case of two-dimensional (2D/2D) and three-dimensional (3D/2D) islands on surfaces [12]. A fairly general derivation of the basic results of the LSW theory based on [10, 11, 12] is given in [14]; let us now briefly repeat the most important steps of this derivation in the particular case of a mixed 3D/2D system in which surface diffusion acts as a limiting process for the island growth.

The LSW theory is a mean-field theory based on the diffusion equation approach. The LSW model assumes that the system is being composed of the ideal adatom gas and an island formed by condensed adatoms; these two phases are considered to be in diffusive equilibrium. This implies that the adatom concentration $n(\rho)$ in the immediate vicinity of an island of radius ρ is given by

$$n(\rho) = n(\infty) \exp \left[\frac{\mu(\rho)}{kT} \right], \quad (1.10)$$

where $n(\infty)$ is the equilibrium concentration at an ideally flat phase boundary between the adatom gas and the bulk material, $\mu(\rho)$ is the chemical potential of an island, which is considered to be dependent on the island radius, k is the Boltzmann's constant and T is the temperature.

²However, this extension is based on several assumptions of doubtful validity; a better treatment can be found in [13].

1.4.1 The growth rate equation

The starting point is the equation for the growth rate for hemispherical island centered in the origin of the coordinate system

$$\frac{dV}{dt} = \frac{d}{dt} \left[\frac{2\pi}{3} \rho^3 \right] = -v_M \int_{\mathcal{C}} \mathbf{J} \cdot \hat{\mathbf{n}} d\gamma, \quad (1.11)$$

where v_M is the molar volume of the material in the island, \mathbf{J} is the adatom flux, \mathcal{C} is the curve encircling the base of the island, $\hat{\mathbf{n}}$ is the outward normal to the curve \mathcal{C} and $d\gamma$ is the line element of \mathcal{C} . If \mathbf{J} is constant around the periphery of the island and parallel to $\hat{\mathbf{n}}$, then

$$\frac{d}{dt} \left[\frac{2\pi}{3} \rho^3 \right] = -2\pi\rho v_M J. \quad (1.12)$$

The adatom flux is, according to Fick's first law, $\mathbf{J} = -\mathcal{D}\nabla n$, where \mathcal{D} is the adatom diffusivity, and thus

$$\frac{d}{dt} \left[\frac{2\pi}{3} \rho^3 \right] = 2\pi\rho v_M \mathcal{D} |\nabla n|_{\mathbf{r}=\rho}. \quad (1.13)$$

The two-dimensional diffusion equation has now to be solved in order to evaluate the concentration field gradient $|\nabla n|$. We have already stated that the steady-state solution to the 2D diffusion equation has a logarithmic divergence which has to be dealt with. Chakravery [12] used a screening length concept to circumvent the problem of diverging concentration field to obtain

$$|\nabla n|_{\mathbf{r}=\rho} = \frac{\bar{n} - n(\rho)}{\rho \ln(\ell/\rho)} \quad (1.14)$$

where \bar{n} is the equilibrium adatom concentration far from the island and ℓ is the screening length. It has been argued [4] that this treatment is unsatisfactory and should not be taken too seriously; we shall use it nevertheless since all the other models are significantly more complicated. Substituting (1.14) into (1.13) we obtain

$$\frac{d}{dt} \left[\frac{2\pi}{3} \rho^3 \right] = \frac{2\pi v_M \mathcal{D}}{\ln(\ell/\rho)} [\bar{n} - n(\rho)] \approx \frac{2\pi v_M \mathcal{D}}{\ln \tilde{\ell}} [\bar{n} - n(\rho)] \quad (1.15)$$

where we have approximated $\ln(\ell/\rho)$ by a constant $\ln \tilde{\ell}$ [14]. Rearranging (1.15) we get

$$\frac{d\rho}{dt} = \frac{v_M \mathcal{D}}{\rho^2 \ln \tilde{\ell}} [\bar{n} - n(\rho)]. \quad (1.16)$$

From (1.16) it is evident that the growth rate is proportional to the supersaturation $\bar{n} - n(\rho)$. The *critical island radius* is defined as the radius ρ^* of an island that does not grow nor shrink,

$$n(\rho^*) \equiv \bar{n} = \exp \left[\frac{\mu(\rho^*)}{kT} \right]. \quad (1.17)$$

If $\mu(\rho)$ is a monotonic function of ρ , as we shall assume from now on, then ρ^* is unique.

An appropriate form of the chemical potential has to be chosen if one wants to proceed further. In order to preserve dynamical scaling, the expression for the chemical potential has to be of the form

$$\mu(\rho) = cr^{-\alpha}, \quad (1.18)$$

where c is a constant and $\alpha \geq 1$. The exponent α comes from the expression for the Gibbs free energy of the island and the thermodynamic identity $\mu = (\partial G / \partial n)$. In the most commonly considered case of *capillarity-driven coarsening*, the driving force for ripening is the reduction of the total surface energy of the islands, which corresponds to $\mu(\rho) \sim \gamma \partial S / \partial V \sim \gamma \rho^{-1}$, where γ is the surface tension (surface energy per unit area); hence, $\alpha = 1$ for capillarity-driven coarsening.

The usual practice is to expand the exponentials in (1.17) into their Taylor series and to retain only the absolute and linear terms, which corresponds to the case of low supersaturations and/or high temperatures; the growth law (1.16) in this approximation with $\mu(\rho)$ given by (1.18) then reads

$$\frac{d\rho}{dt} = \frac{K}{\rho^2} \left(\frac{1}{(\rho^*)^\alpha} - \frac{1}{\rho^\alpha} \right) \quad (1.19)$$

with K being a constant. It is convenient to define the following quantities in order to simplify the following calculations: the *relative radius*

$$u(t) = \frac{\rho(t)}{\rho^*(t)}, \quad (1.20)$$

the *dimensionless time*

$$\tau = 4K \ln \left(\frac{\rho^*(t)}{\rho^*(0)} \right), \quad (1.21)$$

where $\rho^*(0)$ is the critical radius for the system at $t = 0$, and the *growth parameter*

$$\nu = 4K \frac{dt}{d[(\rho^*)^4]}. \quad (1.22)$$

Using (1.20), (1.21) and (1.22), the growth equation can be cast into the dimensionless form

$$\frac{du}{d\tau} = \frac{1}{4u^3} [\nu(u - 1) - u^4]. \quad (1.23)$$

1.4.2 Mean island radius

Equation (1.22) can be used to find the expression for the time evolution of the critical island radius. If the growth parameter ν is independent of time, we get, after integration,

$$[\rho^*(t)]^4 = [\rho^*(0)]^4 + \frac{4}{\nu} K t. \quad (1.24)$$

Since the critical radius is equal to the mean island radius, the mean island radius grows, for large t , as

$$\langle \rho \rangle \sim t^{1/4}. \quad (1.25)$$

1.4.3 Conservation of mass

The theory presented in [14] is valid (apart from some very special cases) only in the case of zero deposition flux, i.e., in mass-conserved systems. The requirement of mass conservation can be stated, for hemispherical islands, in the form

$$\int_0^{\infty} \frac{2\pi}{3} \rho^3 \phi(\rho, t) d\rho = V_0, \quad (1.26)$$

where $\phi(\rho, t)$ is the distribution function for the island radii and V_0 is the total volume of all islands.

In scaled variables (1.20), (1.21) and (1.22), the mass conservation condition (1.26) becomes

$$\int_0^{\infty} u^3 \phi(u, \tau) du = Q \quad (1.27)$$

where Q is a constant and $\phi(u, \tau)$ is the scaled distribution function. We shall assume that $\phi(u, \tau)$ can be written in a separated form

$$\phi(u, \tau) = F(u)T(\tau). \quad (1.28)$$

Substituting this into (1.27) and using (1.21) we get

$$T(\tau) = \exp\left(-\frac{3}{4}\tau\right). \quad (1.29)$$

1.4.4 The equation of continuity

The third and last of the equations necessary to establish the LSW theory is the equation of continuity for the distribution function

$$\frac{\partial \phi}{\partial \tau} + \frac{\partial}{\partial u} \left[\phi \frac{d\phi}{d\tau} \right] = 0 \quad (1.30)$$

which comes from the fact that island radii change smoothly in time, i.e., nucleation and island coalescence are prohibited. Substituting (1.28) and (1.29) into the equation of continuity we arrive at an equation for the spatial part $F(u)$ of the distribution function

$$F(u) = -\frac{1}{f(u)} \exp\left[\frac{3}{4} \int_0^u \frac{1}{f(u')} du'\right] \quad (1.31)$$

where $f(u) = du/d\tau$ is given by equation (1.23).

However, equation (1.23) still contains the unknown growth parameter ν . The value of ν_0 corresponding to the LSW solution is determined by the solution of simultaneous equations

$$f(u_0)|_{\nu=\nu_0} = 0, \quad f'(u_0)|_{\nu=\nu_0} = 0, \quad (1.32)$$

where u_0 is the value of u above which $F(u)$ vanishes. The two parameters ν_0 and u_0 are given by

$$\nu_0 = \frac{4^4}{3^3} = \frac{256}{27}, \quad u_0 = \frac{4}{3}. \quad (1.33)$$

The plot of $F(u)$ is in the figure 1.1.

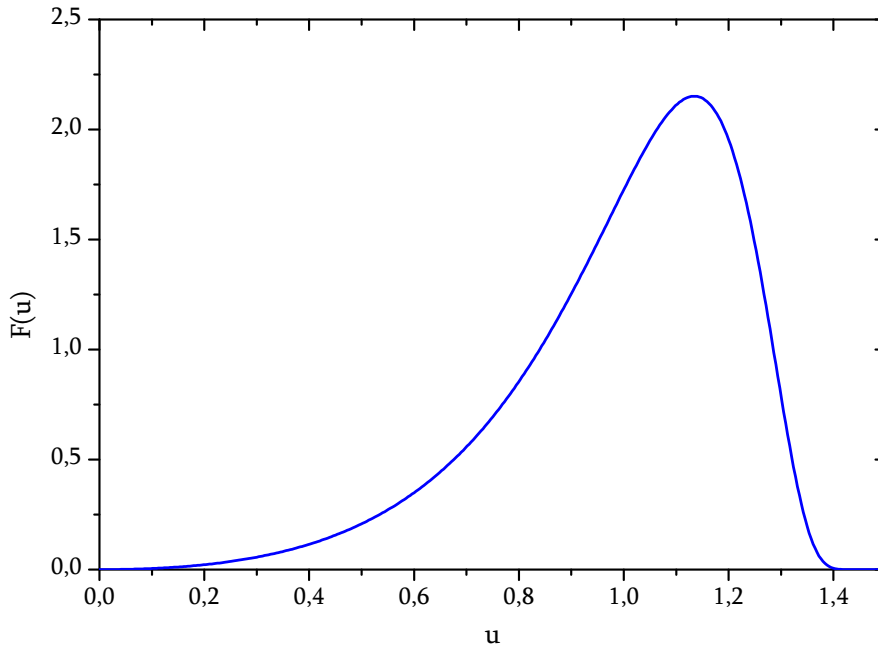


Figure 1.1: The time-independent part $F(u)$ of the scale-invariant LSW distribution function $\phi(u, \tau) = F(u)T(\tau)$.

1.5 A many-body theory for 3D/2D systems

The LSW theory is a mean-field model and it is thus strictly valid only in the limit of zero areal coverage. Our goal is to obtain a theoretical prediction of behavior of a mass-conserved system with high areal coverage where island-island interactions are important. We therefore employed a many-body theory based on the diffusion equation approach [7]. This theory was originally developed for 3D/3D and 2D/2D systems and slight adjustments were therefore required if we wanted to apply it for 3D/2D systems. Unfortunately, the resulting equations are far too complex to be solved analytically, and we had to resort to numerical solution, or, as we will say from now on, to numerical simulation of the time evolution of the system.

1.5.1 Basic equations for the numerical simulation

The starting point of our treatment of the ripening problem is the 2D steady-state diffusion equation³ for the adatom concentration field

$$\Delta n(\mathbf{r}) = 0 \tag{1.34}$$

³In the quasistationary approximation, in which we neglect the time derivative $\partial n/\partial t$. This can be done if the growth rate of islands is much slower than the relaxation time of concentration field [7].

subject to the boundary condition

$$n(\mathbf{r})|_{|\mathbf{r}-\mathbf{R}_j|=\rho_j} = n(\infty) \exp \left[\frac{\mu(\rho_j)}{kT} \right] \quad (1.35)$$

on the perimeter of the j th island, $j = 1, \dots, N$, and the boundary condition

$$\lim_{|\mathbf{r}| \rightarrow \infty} n(\mathbf{r}) = \bar{n} \quad (1.36)$$

which specifies the concentration field far from the islands. We shall assume that coarsening is capillarity-driven, leading to the chemical potential of the form [15]

$$\mu(\rho) = \frac{\gamma v_M}{N_A} \frac{\partial S}{\partial V} = \frac{2\gamma v_M}{N_A \rho} = \frac{\sigma}{\rho}, \quad (1.37)$$

where γ is the surface tension, v_M is the molar volume of the island phase, N_A is Avogadro's constant, S is the island surface, V is the island volume and $\sigma = 2\gamma v_M / N_A kT$ is the *capillary length*. We can Taylor-expand the exponential in (1.35) and retain only terms up to the first order in μ/kT , following the same line of thought as in section 1.4.1, to get

$$n(\mathbf{r})|_{|\mathbf{r}-\mathbf{R}_j|=\rho_j} = n(\infty) \left[1 + \frac{\sigma}{\rho} \right], \quad (1.38)$$

the Gibbs-Thomson boundary condition.

Let us now define the following *characteristic quantities*: *characteristic length* $r_c = \sigma$, *characteristic time* $t_c = \sigma^3 / v_M \mathcal{D}n(\infty)$ and *dimensionless concentration field* $\phi(\mathbf{r}) = [n(\mathbf{r}) - n(\infty)] / n(\infty)$. Using these, we can rewrite equations (1.34), (1.38) and (1.36) in the dimensionless form

$$\Delta \phi(\mathbf{r}) = 0, \quad (1.39)$$

$$\phi(\mathbf{r})|_{|\mathbf{r}-\mathbf{R}_j|=\rho_j} = 1/\rho, \quad (1.40)$$

$$\lim_{|\mathbf{r}| \rightarrow \infty} \phi(\mathbf{r}) = \bar{\phi}. \quad (1.41)$$

Equations (1.39), (1.40) and (1.41) define a many-body diffusion problem which is not feasible without approximations.

Yao [7] replaced each island by a point source (or sink) of strength B located at the point \mathbf{R} . This is a good approximation provided that the islands are immobile and well separated in space, limiting the applicability of the theory to areal coverages lesser than approximately 0,1 [7]. Equation (1.39) can be then defined even inside the original islands,

$$\Delta \phi(\mathbf{r}) = 2\pi \sum_{j=1}^N B_j \delta(\mathbf{r} - \mathbf{R}_j). \quad (1.42)$$

We need two more equations to be able to solve (1.42): the growth rate equation and the mass conservation law. We begin with the growth rate equation (1.11)

$$\frac{d}{dt} \left[\frac{2\pi}{3} \rho_j^3 \right] = - \int_{c_j} \mathbf{J} \cdot \hat{\mathbf{n}} d\gamma. \quad (1.43)$$

According to the Fick's first law, the diffusion flux \mathbf{J} is proportional to the negatively taken gradient of the concentration field ϕ ; in our dimensionless variables, the constant of proportionality is equal to one and thus $\mathbf{J} = -\nabla\phi$. Substituting this into (1.43) and using the divergence theorem to transform the contour integral into surface integral gives, using (1.42),

$$\frac{d}{dt} \left[\frac{2\pi}{3} \rho_j^3 \right] = - \int_{S_j} \Delta\phi(\mathbf{r}) dS = 2\pi B_j, \quad (1.44)$$

and hence

$$\frac{d\rho_j}{dt} = B_j \rho_j^{-2}. \quad (1.45)$$

Finally, the mass conservation law is

$$\sum_{j=1}^N B_j = 0. \quad (1.46)$$

We will see in the next section that the treatment of Ostwald ripening using the diffusion equation stands and falls with the conservation of mass (1.46).

1.5.2 Solution of the diffusion equation

Equation (1.42) can be solved using the method of Green's functions. The Green's function of Poisson's equation $\Delta\phi(\mathbf{r}) = f(\mathbf{r})$ in two dimensions is

$$G(\mathbf{r}, \mathbf{r}') = \frac{1}{2\pi} \ln |\mathbf{r} - \mathbf{r}'|. \quad (1.47)$$

The solution to (1.42) is then

$$\phi(\mathbf{r}) = \int_{\mathbf{r}'} G(\mathbf{r}, \mathbf{r}') f(\mathbf{r}') d\mathbf{r}' = B_0 + \sum_{j=1}^N B_j \ln |\mathbf{r} - \mathbf{R}_j| \quad (1.48)$$

with B_0 constant. The Gibbs-Thomson boundary condition (1.40) becomes

$$B_0 + B_j \ln \rho_j + \sum_{i \neq j}^N B_i \ln |\mathbf{r} - \mathbf{R}_i| = \rho_j^{-1} \quad \text{for } |\mathbf{r} - \mathbf{R}_j| = \rho_j. \quad (1.49)$$

The expression $|\mathbf{r} - \mathbf{R}_i|$ in the last term on the right-hand side is very inconvenient and we shall therefore get rid of it using the so-called *monopolar approximation* [7, 16]. First, we expand this expression into the Fourier series (see figure 1.2)

$$\begin{aligned} |\mathbf{r} - \mathbf{R}_i| &= \sqrt{\rho_j^2 - 2\rho_j |\mathbf{R}_j - \mathbf{R}_i| \cos \psi(\mathbf{r}) + (\mathbf{R}_j - \mathbf{R}_i)^2} = \\ &= A_0 + \sum_{n=1}^{\infty} A_n \cos(n\psi) + B_n \sin(n\psi). \end{aligned} \quad (1.50)$$

Second, we evaluate the coefficient A_0 as usual by multiplying both sides by A_0 and integrating over ψ from 0 to 2π with the result

$$A_0 = |\mathbf{R}_j - \mathbf{R}_i|. \quad (1.51)$$

Third, we truncate the series at A_0 , giving

$$|\mathbf{r} - \mathbf{R}_i| \approx |\mathbf{R}_j - \mathbf{R}_i| \quad \text{for } |\mathbf{r} - \mathbf{R}_j| = \rho_j. \quad (1.52)$$

This approximation is valid when the other islands are distributed evenly around the j th island, so that the anisotropy in $|\mathbf{r} - \mathbf{R}_i|$ averages over. We will consider higher-order approximations later. Using the monopolar approximation, (1.49) becomes

$$B_0 + B_j \ln \rho_j + \sum_{i \neq j}^N B_i \ln |\mathbf{R}_j - \mathbf{R}_i| = \rho_j^{-1} \quad \text{for } |\mathbf{r} - \mathbf{R}_j| = \rho_j. \quad (1.53)$$

The growth rates can be evaluated by solving equation (1.53) together with the conservation of mass (1.46).

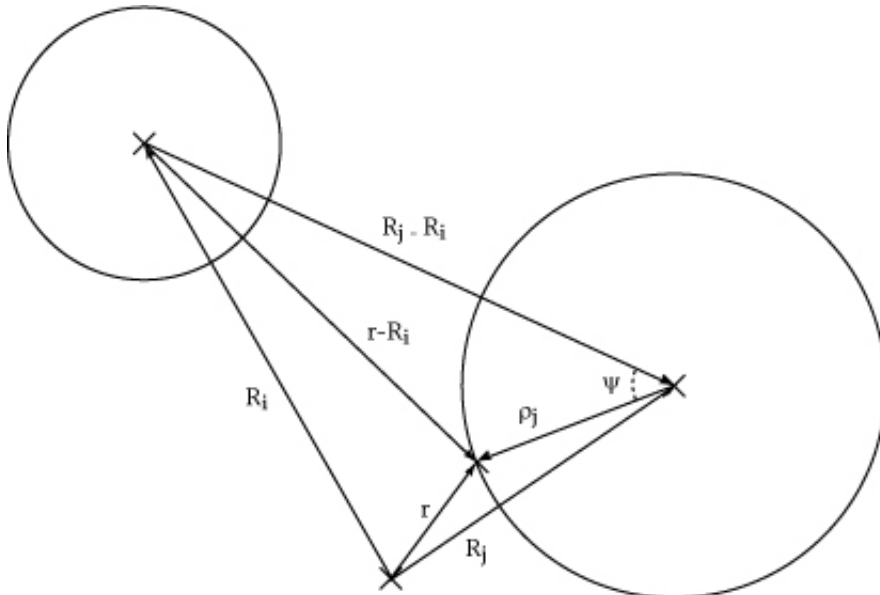


Figure 1.2: To the monopole approximation.

1.5.3 The Ewald summation technique

Equations (1.46) and (1.53) are sufficient to find the growth rates. However, the last term on the left-hand side of equation (1.53), the *interaction term*, contains logarithm of the interparticle separation; this implies that the interactions between the islands are extremely long-ranged. We should be therefore very careful when evaluating the interaction term, because its value depends sensitively even on the islands very far away (which means instability with respect to numerical roundoff in the simulation). An elegant way to get rid of the problems with long-ranged interactions is to use the so-called *Ewald summation*. The idea is very simple: we split the interaction between the islands into short-ranged and long-ranged part and then sum the short-ranged part in direct space and the long-ranged part in reciprocal space where it converges very rapidly.

Let us then split $\phi(\mathbf{r})$ into two parts $\phi_1(\mathbf{r})$ and $\phi_2(\mathbf{r})$, which are found by solving equations

$$\Delta\phi_1(\mathbf{r}) = 2\eta \sum_{i=1}^N B_i \exp[-\eta|\mathbf{r} - \mathbf{R}_i|^2], \quad (1.54)$$

$$\Delta\phi_2(\mathbf{r}) = -2\eta \sum_{i=1}^N B_i \exp[-\eta|\mathbf{r} - \mathbf{R}_i|^2] + 2\pi \sum_{i=1}^N B_i \delta(\mathbf{r} - \mathbf{R}_i), \quad (1.55)$$

where $\eta > 0$ is a constant yet to be determined. It is evident that the sum $\phi = \phi_1 + \phi_2$ is the solution of the original problem (1.42). Equation (1.54) is solved using the Fourier transform method. If $\Phi_1(\mathbf{k})$ is the Fourier transform of $\phi_1(\mathbf{r})$,

$$\phi_1(\mathbf{r}) = \frac{1}{(2\pi)^2} \int_{\mathbf{k}} \Phi_1(\mathbf{k}) \exp(\mathbf{i}\mathbf{k} \cdot \mathbf{r}) \, d\mathbf{k}, \quad (1.56)$$

then

$$\Delta\phi_1(\mathbf{r}) = -\frac{1}{(2\pi)^2} \int_{\mathbf{k}} k^2 \Phi_1(\mathbf{k}) \exp(\mathbf{i}\mathbf{k} \cdot \mathbf{r}) \, d\mathbf{k} \quad (1.57)$$

and thus the Fourier image of $\Delta\phi_1(\mathbf{r})$ is $k^2\Phi_1(\mathbf{k})$. Fourier transforming the right-hand side of (1.54) we get

$$\int_{\mathbf{r}} 2\eta \sum_{i=1}^N B_i \exp[-\eta(\mathbf{r} - \mathbf{R}_i)^2 - \mathbf{i}\mathbf{k} \cdot \mathbf{r}] \, d\mathbf{r} = 2\pi \sum_{i=1}^N B_i \exp[-\mathbf{i}\mathbf{k} \cdot \mathbf{R}_i] \exp\left[-\frac{k^2}{4\eta^2}\right]. \quad (1.58)$$

From this and (1.57) we get $\phi_1(\mathbf{r})$ as

$$\phi_1(\mathbf{r}) = -\frac{1}{2\pi} \sum_{i=1}^N B_i \int_{\mathbf{k}} k^{-2} \exp\left[-\frac{k^2}{4\eta^2}\right] \exp[\mathbf{i}\mathbf{k} \cdot (\mathbf{r} - \mathbf{R}_i)] \, d\mathbf{k}. \quad (1.59)$$

The solution of (1.55) can be found using the Green's function (1.47),

$$\phi_2(\mathbf{r}) = \int_{\mathbf{r}'} \frac{1}{2\pi} \ln|\mathbf{r} - \mathbf{r}'| \left\{ 2\eta \sum_{i=1}^N B_i \exp[-\eta|\mathbf{r} - \mathbf{R}_i|^2] + 2\pi \sum_{i=1}^N B_i \delta(\mathbf{r} - \mathbf{R}_i) \right\} d\mathbf{r}'. \quad (1.60)$$

We have already evaluated the second part of this integral involving the δ -functions; to evaluate the first part, we transform the integral into polar coordinates and integrate the radial integral by parts to obtain

$$\phi_2(\mathbf{r}) = -\frac{1}{2\pi} \sum_{i=1}^N B_i \int_0^\infty \exp(-\eta r'^2) \int_0^{2\pi} \frac{r' - |\mathbf{r} - \mathbf{R}_i| \cos \theta}{|r' - (\mathbf{r} - \mathbf{R}_i)|^2} \, d\theta dr'. \quad (1.61)$$

The angular integral is $2\pi/r'$ for $r' > |\mathbf{r} - \mathbf{R}_i|$ and zero for $r' \leq |\mathbf{r} - \mathbf{R}_i|$. Equation (1.61) thus becomes

$$\phi_2(\mathbf{r}) = -\sum_{i=1}^N B_i \int_{|\mathbf{r}-\mathbf{R}_i|}^\infty \frac{\exp(-\eta r'^2)}{r'} \, dr'. \quad (1.62)$$

Adding (1.59) and (1.62) we get

$$\phi(\mathbf{r}) = -\frac{1}{2\pi} \sum_{i=1}^N B_i \int_{\mathbf{k}} k^{-2} \exp\left[-\frac{k^2}{4\eta^2}\right] \exp[\mathbf{ik} \cdot (\mathbf{r} - \mathbf{R}_i)] d\mathbf{k} - \sum_{i=1}^N B_i \int_{|\mathbf{r}-\mathbf{R}_i|}^{\infty} \frac{\exp(-\eta r'^2)}{r'} dr'. \quad (1.63)$$

We now need to apply the Gibbs-Thomson boundary condition (1.53). We begin by rewriting (1.53) as

$$\rho_j^{-1} = B_0 + B_j \ln \rho_j + \lim_{\mathbf{R}'_j \rightarrow \mathbf{R}_j} \left[-B_j \ln |\mathbf{R}'_j - \mathbf{R}_j| + \sum_{i=1}^N |\mathbf{R}'_j - \mathbf{R}_i| \right]. \quad (1.64)$$

The last term in the square bracket is, apart from a constant B_0 , nothing more than the original solution (1.48), and thus

$$\rho_j^{-1} = B_0 + B_j \ln \rho_j + \lim_{\mathbf{R}'_j \rightarrow \mathbf{R}_j} \left[-B_j \ln |\mathbf{R}'_j - \mathbf{R}_j| - B_0 + \phi(\mathbf{R}'_j) \right]. \quad (1.65)$$

The trick is that now we can substitute (1.63) for $\phi(\mathbf{r})$ in this equation; after quite lengthy rearrangements involving the treatment of limits and several transformations of integrals we get [7]

$$\begin{aligned} \rho_j^{-1} = & B_0 + B_j \left[\ln(\sqrt{\eta} \rho_j) + \int_0^1 \frac{1 - \exp(-t^2)}{t} dt - \int_1^{\infty} \frac{\exp(-t^2)}{t} dt \right] - \\ & - \sum_{i \neq j}^N B_i \int_{\sqrt{\eta} |\mathbf{R}_j - \mathbf{R}_i|}^{\infty} \frac{\exp(-t^2)}{t} dt - \frac{1}{2\pi} \sum_{i=1}^N B_i \int_{\mathbf{k}} \frac{\exp(-k^2/4\eta)}{k^2} \exp[\mathbf{ik} \cdot (\mathbf{R}_j - \mathbf{R}_i)] d\mathbf{k}. \end{aligned} \quad (1.66)$$

The last approximation required is that we restrict the system to a square of a side L and use periodic boundary conditions. The Fourier transform in (1.66) reduces to Fourier series and the unknown constant η relates to the system size, $\eta = 1/L^2$. The allowed values of \mathbf{k} are $\mathbf{k} = 2\pi(n_x, n_y)/L$ with n_x, n_y integer. Equation (1.66) becomes

$$\begin{aligned} \rho_j^{-1} = & B_0 + B_j \left[\ln\left(\frac{\rho_j}{L}\right) + \int_0^1 \frac{1 - \exp(-t^2)}{t} dt - \int_1^{\infty} \frac{\exp(-t^2)}{t} dt \right] - \\ & - \sum_{i \neq j}^N B_i \int_{|\mathbf{R}_j - \mathbf{R}_i|/L}^{\infty} \frac{\exp(-t^2)}{t} dt - \frac{1}{2\pi} \sum_{i=1}^N B_i \sum_{\mathbf{k} \neq 0} \frac{\exp(-k^2/4L^2)}{k^2} \exp[\mathbf{ik} \cdot (\mathbf{R}_j - \mathbf{R}_i)]. \end{aligned} \quad (1.67)$$

The singularity corresponding to $\mathbf{k} = 0$ is resolved thanks to the conservation law (1.46). Equations (1.45), (1.46) and (1.67) are all what is needed for the simulation.

1.5.4 Scaling properties of simulation equations

Suppose we rescale the spatial dimensions of the system by a factor α , e. g., $L \rightarrow \alpha L$, $\rho \rightarrow \alpha \rho$ and so on. The growth rates B_i , which are given by equation (1.67), are rescaled to $B_i \rightarrow B_i/\alpha$ since each B_i is a linear function of $1/\rho_j$'s. If we also rescale the time as

$t \rightarrow \alpha^4 t$, then the growth equation (1.45) is left unchanged by the scaling. This means that if we have a solution of the simulation equations corresponding to a system of size L and we want to find the solution for a system α -times larger, but otherwise identical, we need only to relabel the axes like

$$\rho \rightarrow \alpha\rho, \quad V \rightarrow \alpha^3 V, \quad t \rightarrow \alpha^4 t. \quad (1.68)$$

Thanks to these scaling properties, the simulation is independent of the computation cell size L . It follows that we can set $L = 1$ in (1.67) and treat all the distances as being relative to the system size.

1.5.5 Matrix form of the simulation equations

Let us now take equations (1.67) and (1.46) and rewrite them in a more compact matrix form. We begin by defining the quantities c_j , d_j , \mathcal{K}_{ij} and \mathcal{S}_{ij} as follows:

$$c_j = \ln\left(\frac{\rho_j}{L}\right) + \int_0^1 \frac{1 - \exp(-t^2)}{t} dt - \int_1^\infty \frac{\exp(-t^2)}{t} dt, \quad (1.69)$$

$$d_j = \rho_j^{-1}, \quad (1.70)$$

$$\mathcal{K}_{ij} = - \int_{\frac{|\mathbf{R}_j - \mathbf{R}_i|}{L}}^\infty \frac{\exp(-t^2)}{t} dt, \quad (1.71)$$

$$\mathcal{S}_{ij} = -2\pi \sum_{\mathbf{k} \neq 0} \frac{\exp(-k^2 L^2/4)}{k^2 L^2} \exp[i\mathbf{k} \cdot (\mathbf{R}_j - \mathbf{R}_i)]. \quad (1.72)$$

Using definitions (1.69), (1.70), (1.71) and (1.72) and noting that $\mathcal{S}_{ij} = \mathcal{S}_{ji}$, $\mathcal{K}_{ij} = \mathcal{K}_{ji}$ we can write the set of $(N + 1)$ simultaneous linear equations (1.67) and (1.46) in the desired matrix form

$$\begin{pmatrix} 0 & 1 & 1 & \dots & 1 \\ 1 & c_1 + \mathcal{S}_{1,1} & \mathcal{K}_{1,2} + \mathcal{S}_{1,2} & \dots & \mathcal{K}_{1,N} + \mathcal{S}_{1,N} \\ 1 & \mathcal{K}_{1,2} + \mathcal{S}_{1,2} & c_2 + \mathcal{S}_{2,2} & \dots & \mathcal{K}_{2,N} + \mathcal{S}_{2,N} \\ \vdots & \vdots & \vdots & \ddots & \vdots \\ 1 & \mathcal{K}_{1,N} + \mathcal{S}_{1,N} & \mathcal{K}_{2,N} + \mathcal{S}_{2,N} & \dots & c_N + \mathcal{S}_{N,N} \end{pmatrix} \begin{pmatrix} B_0 \\ B_1 \\ B_2 \\ \vdots \\ B_N \end{pmatrix} = \begin{pmatrix} 0 \\ d_1 \\ d_2 \\ \vdots \\ d_N \end{pmatrix}. \quad (1.73)$$

The coefficient matrix of this linear equation set is symmetric and indefinite.

Chapter 2

The simulation algorithm

2.1 The initial set of islands

Crucial fact that has not been considered so far is that we need an initial condition to solve equations (1.73) and (1.67). By this we mean that we need to know the exact state of the system, i. e., the island positions and radii, at $t = 0$. Since we do not intend to perform simulations of early stages of the ripening (nucleation and coalescence) we have to use a different approach to obtain the initial condition.

2.1.1 Initial distribution of island sizes

We use the spatial (time-independent) part of the LSW size distribution $F(u)$ (1.31) as an initial guess for the island size distribution function. In the first step we need to find the normalized cumulative distribution function

$$\Phi(u) = \frac{1}{\Phi_0} \int_0^u F(u') du', \quad \Phi_0 = \int_0^\infty F(u) du, \quad (2.1)$$

which gives the probability to find an island with relative radius lesser than or equal to u . This function can be found by simple numeric integration of $F(u)$; the corresponding graph can be found in figure 2.1.

In the next step we generate a random number $x \in [0; 1]$ and find the vaule of u corresponding to $x = \Phi(u)$; this procedure is repeated N times in order to get the relative radii $u_i = \rho_i / \langle \rho \rangle$ of N islands to be placed in the simulation cell. Finally, we need to find the average radius $\langle \rho \rangle$. This can be done if we specify the desired areal coverage Θ since

$$\Theta = \frac{1}{L^2} \sum_{i=1}^N \pi \rho_i^2 = \pi \frac{\langle \rho \rangle^2}{L^2} \sum_{i=1}^N \left(\frac{\rho_i}{\langle \rho \rangle} \right)^2 = \pi \frac{\langle \rho \rangle^2}{L^2} \sum_{i=1}^N u_i^2 \quad (2.2)$$

and thus

$$\langle \rho \rangle = \frac{\Theta L^2}{\pi \sum_i u_i^2}. \quad (2.3)$$

The value of $\langle \rho \rangle$ is then used to find the absolute radii $\rho_i = u_i \langle \rho \rangle$.

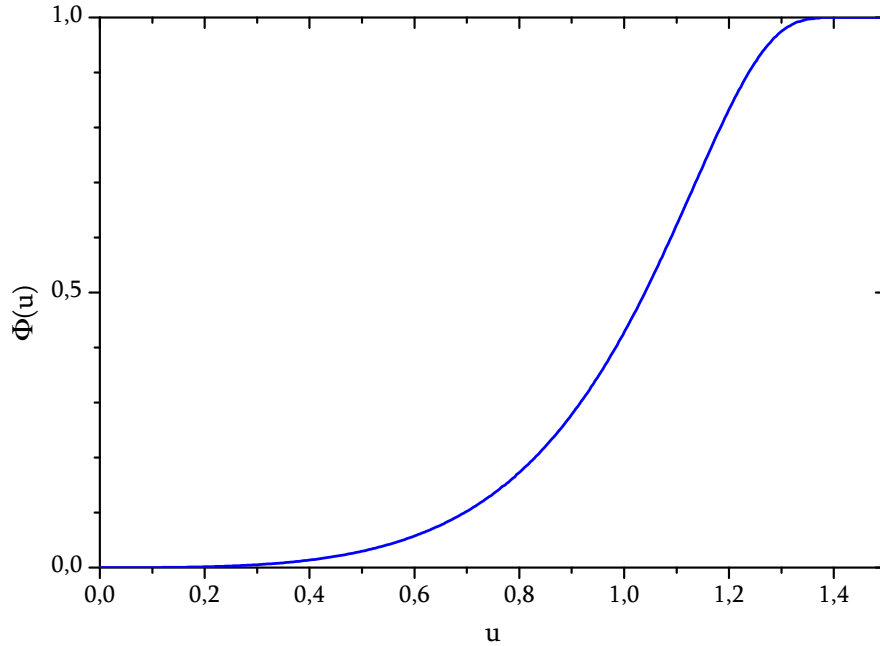


Figure 2.1: The cumulative distribution function $\Phi(u)$ of the island radii in the framework of the LSW theory.

2.1.2 Initial island positions

A good starting approximation of the island size distribution analogous to the LSW distribution in the previous section is not known. We use two methods to obtain the initial island positions within the simulation cell: random placement and random placement with denuded zone.

In the first case we proceed as follows: first, we generate a random island position \mathbf{R}_i within the simulation cell and second, we perform a test if the island to be placed would not overlap with any of the islands already present. To do this we find the location \mathbf{R}_j of the nearest island and test if

$$\rho_i + \rho_j > |\mathbf{R}_i - \mathbf{R}_j|. \quad (2.4)$$

If this condition is fulfilled the island is added to the system; otherwise a new random location is calculated and the procedure is repeated.

The case of random deposition with denuded zone is entirely analogous except that the island is added when

$$\alpha(\rho_i + \rho_j) > |\mathbf{R}_i - \mathbf{R}_j| \quad (2.5)$$

where the parameter α determines the extent of the denuded zone around the island. There is not a simple rule to estimate the optimal value of α ; we use $\alpha = 50$ for simulations with initial areal coverage $1,0 \cdot 10^{-4}$ and $\alpha = 2,5$ for simulations with initial

areal coverage $5,0 \cdot 10^{-2}$. The value for $\Theta = 5,0 \cdot 10^{-2}$ is the same as used in [16]. We should not worry about the exact value of α because the asymptotic state of the system should be independent of the initial conditions. The only purpose of α is to provide a better initial condition in order to speed up the convergence.

2.1.3 The asymptotic behavior of the system

We hope that in the course of our simulation the influence of the initial conditions will decrease as the system evolves towards the asymptotic state. In order to access the long-time behavior we need a system which is large enough; approximately 20 000 islands seems to be enough [16]. The time required for one simulation run scales roughly as $N^3 \log N$; the maximum number of islands for which the simulation is feasible with the available hardware is $N \approx 2\,500$ which is far too few to reach the asymptotic state.

A simple way to circumvent this problem is to perform 4^k simulation runs with relatively small number of islands ($N = 1\,000$ in most cases). The results can be then used to assembly 4^{k-1} initial states for the next step by merging four simulation cells from previous step into one larger cell. This process can be repeated k times.

2.2 The initialization part

In the initialization part of the algorithm the coefficient matrix of linear equation set (1.73) is set up. To do this, we need to evaluate c_j (1.69), d_j (1.70), \mathcal{K}_{ij} (1.71) and \mathcal{S}_{ij} (1.72). Evaluation of d_j is straightforward; the only thing we need to consider is that the coefficients d_j will change after every iteration step since the island radii change in every step. The first term in the expression (1.69) for c_j depends on the island radius; it will therefore also change after every iteration of the simulation. The other two terms in (1.69) are just constants; the corresponding integrals have to be evaluated only once and their values can be inserted into the simulation as parameters. Integration was performed using Simpson's method for improper integrals based on the extended midpoint rule [17].

The maximum value of the lower bound in (1.71) is $\sqrt{2}$ when the two islands are placed in the opposite corners of the simulation cell. It is therefore convenient to split the improper integral in (1.71) into two parts,

$$\mathcal{K}_{ij} = - \int_{\frac{|\mathbf{R}_j - \mathbf{R}_i|}{L}}^{\infty} \frac{\exp(-t^2)}{t} dt = - \int_{\frac{|\mathbf{R}_j - \mathbf{R}_i|}{L}}^{\kappa} \frac{\exp(-t^2)}{t} dt - \int_{\kappa}^{\infty} \frac{\exp(-t^2)}{t} dt, \quad (2.6)$$

where $\kappa > \sqrt{2}$ is the breakpoint¹. The first term is quite ordinary definite integral, while the second one is an improper integral, which is much more difficult to compute numerically. With our clever choice of the breakpoint the improper part is independent of i and j and thus needs to be evaluated only once; this was done in exactly the same way as for the analogous integrals in (1.69), i. e., using Simpson's method. The first

¹The actual value used in the simulation is $\kappa = 1,45$.

integral is calculated using the Romberg method of fourth order [17]. It should be noted that evaluation of this integral is the most time-consuming step in the whole simulation and better quadrature methods would give far better performance; in fact, using Gauss-Legendre quadrature, the simulation can be speeded up as much as ten times, but, unfortunately, Gaussian quadrature proved to be highly unstable in this particular case.

Equation (1.72) for \mathcal{S}_{ij} can be simplified using the fact that $\mathbf{k} = \frac{2\pi}{L}(n_x, n_y)$ with n_x, n_y integer:

$$\mathcal{S}_{ij} = -\frac{1}{2\pi} \sum_{n_x, n_y} \frac{\exp[-\pi^2(n_x^2 + n_y^2)]}{n_x^2 + n_y^2} \exp \left[2\pi i \frac{(n_x, n_y) \cdot (\mathbf{R}_j - \mathbf{R}_i)}{L} \right]. \quad (2.7)$$

Furthermore, equation (2.7) has a kind of inversion symmetry, since for each (n_x, n_y) there is also the term $(-n_x, -n_y)$ in the sum. Using this fact, (2.7) can be reduced to

$$\mathcal{S}_{ij} = -\frac{1}{2\pi} \sum_{n_x, n_y} \frac{\exp[-\pi^2(n_x^2 + n_y^2)]}{n_x^2 + n_y^2} \cos \left[\frac{2\pi}{L} (n_x, n_y) \cdot (\mathbf{R}_j - \mathbf{R}_i) \right] \quad (2.8)$$

from which is evident that $\mathcal{S}_{ij} = \mathcal{S}_{ji}$. Let us now estimate how many terms should be included into the sum. The number of points (n_x, n_y) within the distance n from the origin grows as n^2 while their relative weight in the sum decreases exponentially; the sum is therefore convergent. The weight of the terms with $n = 1$ is of the order 10^{-5} ; terms with $n = \sqrt{2}$ have weight $\approx 10^{-9}$ and the points with $n = 2$ are negligible because their weight is approximately 10^{-17} . Therefore only eight points contribute significantly to the sum: $(\pm 1, 0)$, $(0, \pm 1)$ and $(\pm 1, \pm 1)$. These terms can be summed explicitly to give

$$\begin{aligned} \mathcal{S}_{ij} = & -\frac{1}{\pi} \exp(-\pi^2) \left[\cos \frac{2\pi(R_{j,x} - R_{i,x})}{L} + \cos \frac{2\pi(R_{j,y} - R_{i,y})}{L} \right] - \frac{1}{\pi} \exp(-2\pi^2) \times \\ & \times \left[\cos \frac{2\pi(R_{j,x} - R_{i,x} + R_{j,y} - R_{i,y})}{L} + \cos \frac{2\pi(R_{j,x} - R_{i,x} - R_{j,y} + R_{i,y})}{L} \right]. \end{aligned} \quad (2.9)$$

2.3 Finding the growth rates

We need to solve (1.73) in order to find the growth rates B_i . This linear equation set has a coefficient matrix that is symmetric, but indefinite; the most efficient method to solve this type of linear equation set is the *LDL* decomposition². We used the LAPACK [18] routine DSYSV to perform the decomposition. The efficiency of the DSYSV routine relies strongly on the platform-specific implementation of Basic Linear Algebra Subroutines (BLAS). Although generic BLAS from [19] are enclosed with the simulation package we strongly recommend using either the ACML library [20] for AMD processors or the IMKL library [21] for Intel processors.

²Yao [7] used *LU* decomposition to solve (1.73). The *LU* decomposition does not use the symmetry of the coefficient matrix and is therefore much slower (about a factor of four in our case) than *LDL*.

2.4 Updating the island radii

Having computed the growth rates B_j we can focus on solving (1.45). We used explicit Euler method to solve this set of N uncoupled first-order ordinary differential equations:

$$\rho_j(t + \Delta t) = \rho_j(t) + B_j \rho_j^{-2} \Delta t. \quad (2.10)$$

Since explicit Euler method is indeed a primitive one, great care has to be taken in choosing the time increment Δt . We proceeded as follows: we found the fastest shrinking island, i. e., the one with the largest negative change in the relative volume $dV/dt \sim B_j \rho_j^{-3}$. This is not necessarily the smallest one since the growth rates depend on the neighborhood of the particular island. Then we choose the time step so that the fastest shrinking island loses a certain percentage p of its original volume,

$$\Delta t = -p \frac{\rho_{min}^3}{B_{min}}. \quad (2.11)$$

The island radii are then updated according to (2.10). We chose $p = 0,2$ in our simulations.

2.5 Removing islands from the system

When one of the islands becomes too small it is removed from the system. The condition for an island to be removed is

$$V_j < q \langle V \rangle, \quad (2.12)$$

i. e., the relative island volume with respect to the mean island volume is lesser than q . The actual value of q used in our simulations was $q = 0,05$. When an island is removed, its remaining volume is redistributed evenly among the rest of the islands in order to keep the total volume of the islands constant³; the system is then reinitialized with $N - 1$ islands according to section 2.2 and the simulation continues until the specified number of islands is reached. We chose this minimum value to be $N = 350$ since for $N < 300$ the effects related to limited system size were clearly apparent.

2.6 Implementation

The algorithm used to generate the initial set of islands is implemented in the program `Deposit` and the rest of the simulation algorithm is implemented in the `OsSim` program. Both these programs are written in ISO standard Fortran 95 and compiled using either an evaluation copy of Intel Visual Fortran compiler [22] or the G95 compiler [23] available under the GNU license. `Deposit` and `OsSim` can be found, together with their source code, on the CD enclosed.

³Alternatively, we can transfer the material from the disappearing island to its nearest neighbor, since most islands actually disappear by coalescence [2].

2.7 Possible improvements of the algorithm

The maximum number of islands for which the simulation is completed in reasonable time on available hardware⁴ is approximately 1 600 which is too few to access the asymptotic ripening regime [8]. With the following improvements systems consisting of as much as 100 000 islands can be treated efficiently [16].

Most of the computing time is spent on numerical quadrature when evaluating the coefficients \mathcal{K}_{ij} in (2.6). We tried to implement the Gauss-Legendre method to perform the quadrature, but this proved to be numerically unstable in certain cases although it reduced the simulation time by a factor of 10. A more promising way is to improve the implementation of the Romberg method. A parallel version [24] of this algorithm speeds up the simulation by a factor of 2. It is, however, not implemented in the current version of the OsSim package because of conflicts with the LAPACK library which have not yet been fully resolved.

Another way to reduce the computation time is to use the *cutoff distance* concept [8] which is based on the assumption that only a finite number of nearest-neighbor interactions needs to be taken into account since the diffusion field of a particle sufficiently far away is screened out. Adopting this assumption, we can define the cutoff distance r_c and consider only particles closer than r_c when evaluating the growth rate for a given island; this significantly reduces the size of the equation set that has to be solved. The principal problem with this approach is that there is not an explicit formula for the cutoff distance. However, it has been shown that the results do not depend on r_c if it is chosen large enough [8].

Additionally, we can solve the linear equation set for the growth rates by iterative methods rather than direct methods. Akaiwa [6] used the generalized minimal residual method with a preconditioner along with an efficient matrix-vector multiplication algorithm to reduce the time required to solve the equation set by a factor of 2 500 which is really impressive.

The stability of the simulation could be further enhanced if we use a more elaborate way to solve the growth rate equation (1.73) such as the Runge-Kutta-Fehlberg method of fourth order with adaptive step size (RK45). We did not implement this algorithm since there are problems when choosing the proper step size.

⁴Simulation where 1 400 islands are initially placed into the computation cell lasts approximately 7 hours on AMD Athlon 64 3000+ processor and slightly less than 5 hours using a single core of the Intel C2D T6450 processor.

Chapter 3

Results

We performed 96 simulation runs in total in order to estimate the time dependence of the mean island radii, the distributions of island radii, the nearest-neighbor distance distributions and the radial distribution functions. To find the dependence on the initial areal coverage Θ , we performed 16 runs with $\Theta = 0,0001$ and $\Theta = 0,05$ and 4 runs with $\Theta = 0,01$, $\Theta = 0,02$ and $\Theta = 0,10$. To study the effects of the presence of initial denuded zone on the results, another 16 runs for $\Theta = 0,0001$ with $\alpha = 50$ and $\Theta = 0,05$ with $\alpha = 2,5$ were carried out. In all cases the initial number of islands was 1000 and we iterated until the number of islands decreased to approximately 350. An attempt to access the asymptotic behavior was made using the composite simulations¹ with $k = 2$ for $\Theta = 0,0001$ and $\Theta = 0,05$ both with and without the denuded zones. We used the results of the previous (from now on called *single*) runs as the input for these simulations.

3.1 Mean island radius

There are two ways to obtain the scaling exponent in (1.24). The first is to use the asymptotic form (1.25) and take the logarithm of both sides to get

$$\ln\langle\rho\rangle \sim \frac{1}{3} \ln t. \quad (3.1)$$

Thus, if we plot the time dependence of the mean radius in a log-log plot, the slope of the linear part should be equal to the scaling exponent. We could not use this method since there was *no* linear part at all in the data. The second way to obtain the scaling exponent is to fit the measured data with the model function corresponding to (1.24)

$$\langle\rho(t)\rangle = (A + Bt)^{-c} \quad (3.2)$$

where A , B and c are parameters with the following meaning: A is the cube of the initial mean island radius, B is proportional to the growth constant and c is the reciprocal value of the scaling exponent. The fitted curves are in figures 3.1 - 3.11 and the values of the parameter c are summarized in table 3.1.

LSW theory predicts that the scaling exponent is equal to 1/4 and therefore $c = 4$. The values of c obtained from simulations vary between 3,13 and 5,17 with no apparent

¹As described in section 2.1.3.

Θ	c	Θ	c	Θ	c
0,000 1NS	$3,56 \pm 0,03$	0,05NS	$3,13 \pm 0,07$	0,01NS	$3,7 \pm 0,1$
0,000 1NC	$4,14 \pm 0,06$	0,05NC	$5,17 \pm 0,07$	0,02NS	$3,41 \pm 0,08$
0,000 1DS	$3,86 \pm 0,05$	0,05DS	$2,92 \pm 0,06$	0,10NS	$3,3 \pm 0,1$
0,000 1DC	$4,16 \pm 0,06$	0,05DC	$4,81 \pm 0,05$		

Table 3.1: Scaling exponents obtained from the fit of the simulated data for various initial areal coverages Θ either averaged from single runs (S) or from a composite run (C) and with (D) or without (N) denuded zone.

dependence on coverage or the initial population of islands. Furthermore, the values of the parameter A obtained from the fit are several orders of magnitude lower than expected; the attempt to fit the data points using $A = \langle \rho(0) \rangle$ gave very poor results.

This discrepancy between the theory and our simulations has two reasons. First, the theory itself is not strictly valid because of the unsatisfactory treatment of the diverging concentration fields as mentioned earlier. Apart from this, we will show that in this particular case the theory cannot be applied at all since the prediction of the constant scaling exponent is based on the assumption that the growth rate does not depend on time. To see why this is not true, consider the following: the areal coverage is not constant, which is specific to mixed-dimensional systems. Therefore all quantities dependent on the areal coverage either become dependent on time or, if they are already time-dependent, their time dependence becomes more complicated. Second, it has been shown in many studies (see [4] and references therein) that ν depends on areal coverage and therefore, according to our previous reasoning, on time, invalidating the necessary condition for (1.24) to hold.

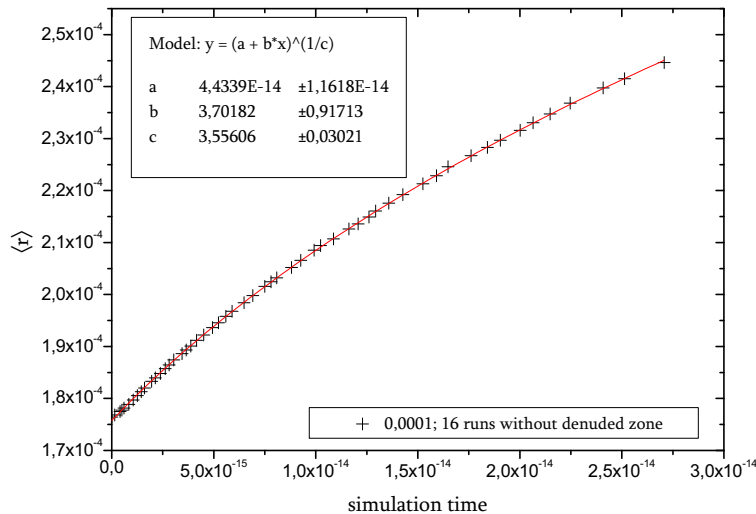


Figure 3.1: Time evolution of the mean island radius for the initial areal coverage $\Theta = 0,0001$ without initial denuded zone (crosses; averaged from 16 single runs) and fit of these data by (3.2) (solid red line).

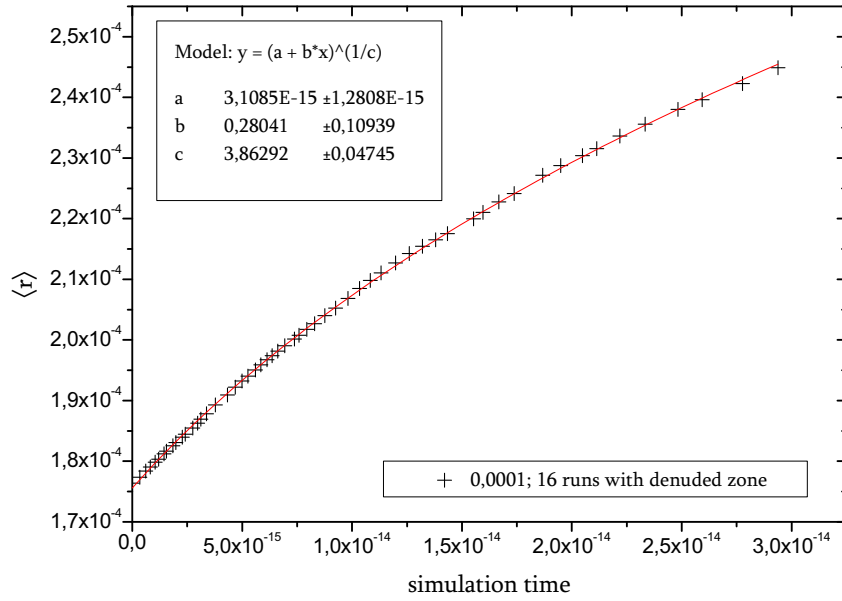


Figure 3.2: Time evolution of the mean island radius for the initial areal coverage $\Theta = 0,0001$ with initial denuded zone (crosses; averaged from 16 single runs) and fit of these data by (3.2) (solid red line).

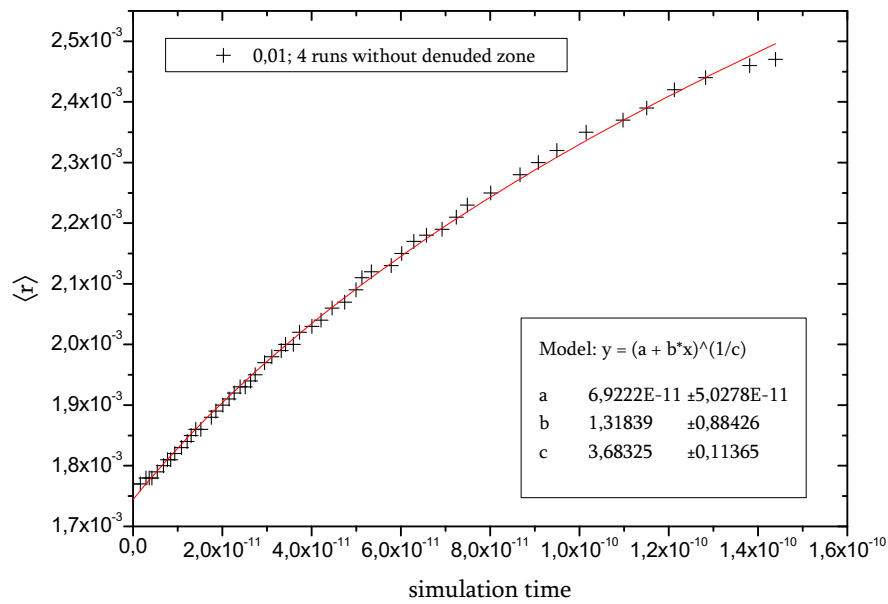


Figure 3.3: Time evolution of the mean island radius for the initial areal coverage $\Theta = 0,01$ without initial denuded zone (crosses; averaged from 4 single runs) and fit of these data by (3.2) (solid red line).

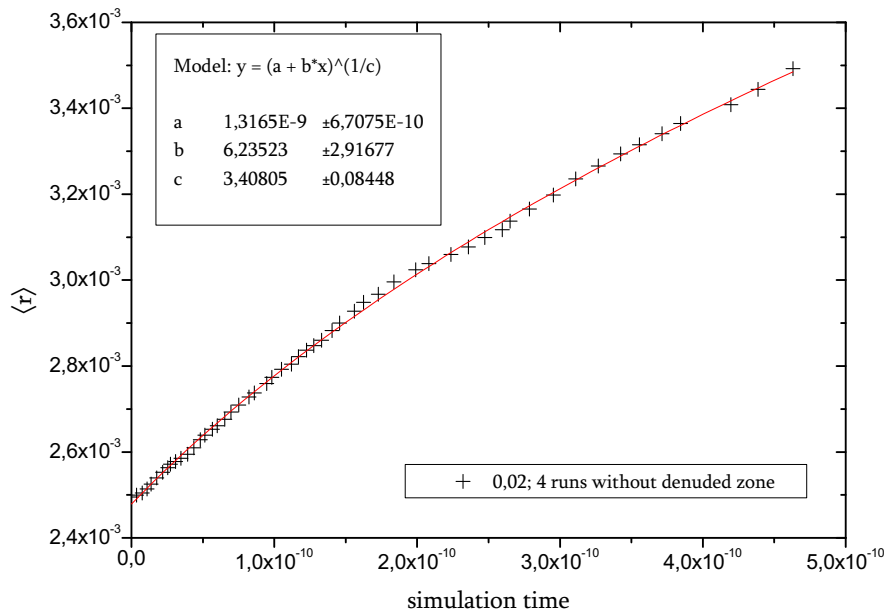


Figure 3.4: Time evolution of the mean island radius for the initial areal coverage $\Theta = 0,02$ without initial denuded zone (crosses; averaged from 4 single runs) and fit of these data by (3.2) (solid red line).

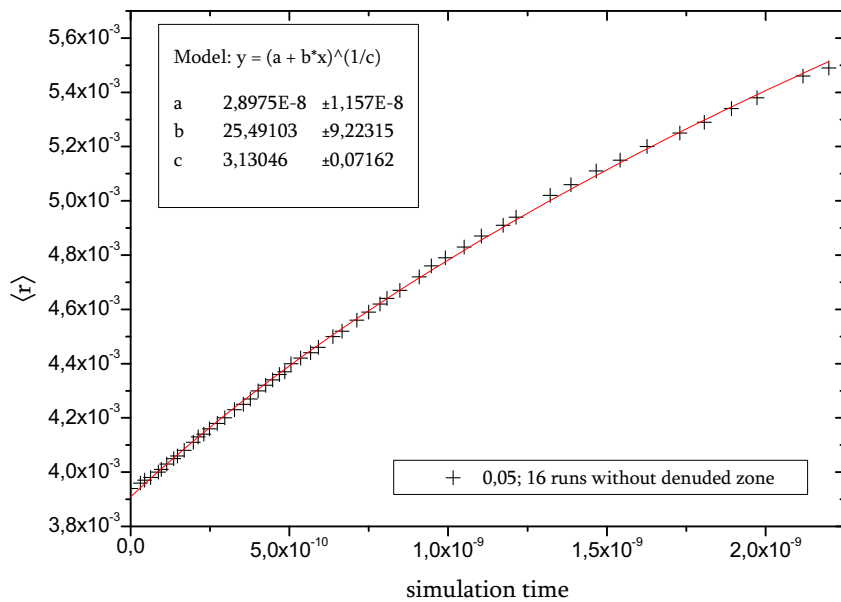


Figure 3.5: Time evolution of the mean island radius for the initial areal coverage $\Theta = 0,05$ without initial denuded zone (crosses; averaged from 16 single runs) and fit of these data by (3.2) (solid red line).

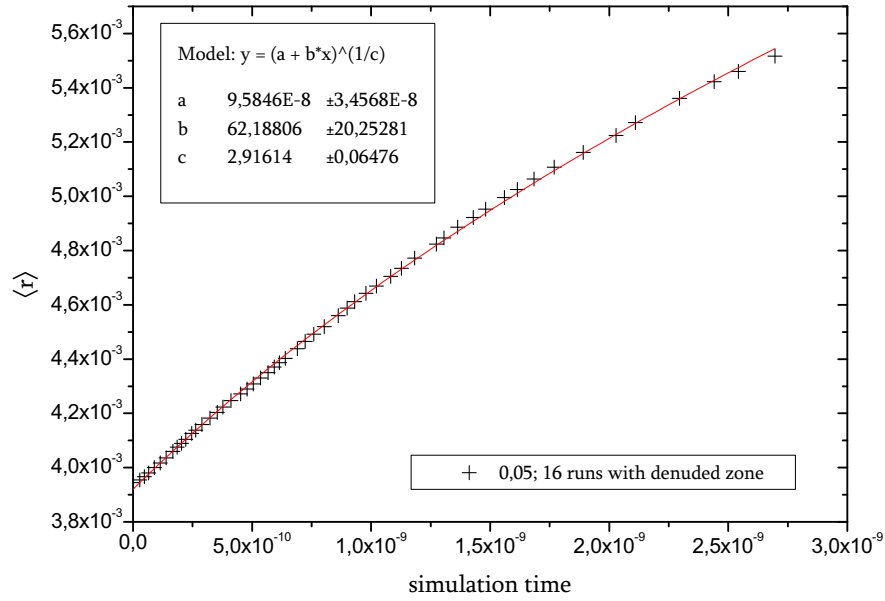


Figure 3.6: Time evolution of the mean island radius for the initial areal coverage $\Theta = 0,05$ with initial denuded zone (crosses; averaged from 16 single runs) and fit of these data by (3.2) (solid red line).

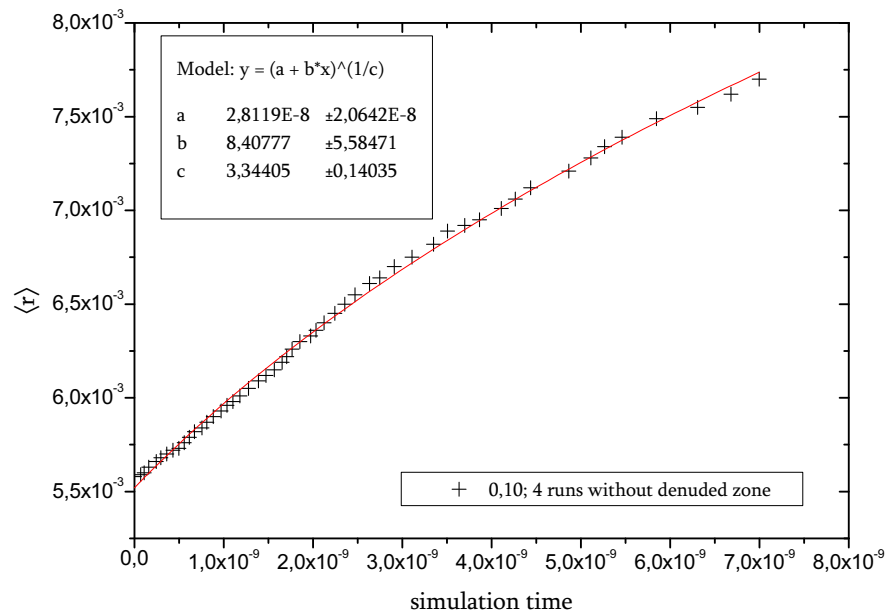


Figure 3.7: Time evolution of the mean island radius for the initial areal coverage $\Theta = 0,10$ without initial denuded zone (crosses; averaged from 4 single runs) and fit of these data by (3.2) (solid red line).

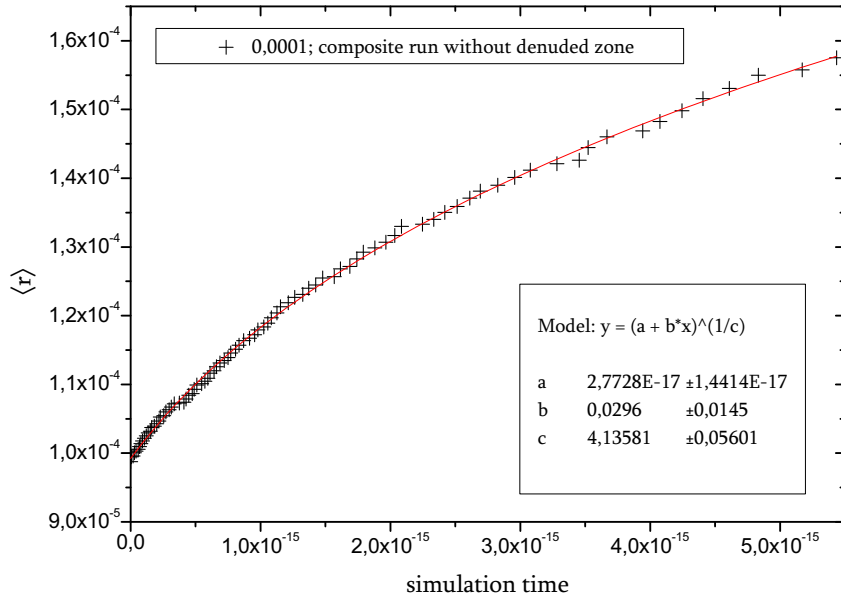


Figure 3.8: Time evolution of the mean island radius for the initial areal coverage $\Theta = 0,0001$ without initial denuded zone (crosses; from composite run with $k = 2$) and fit of these data by (3.2) (solid red line).

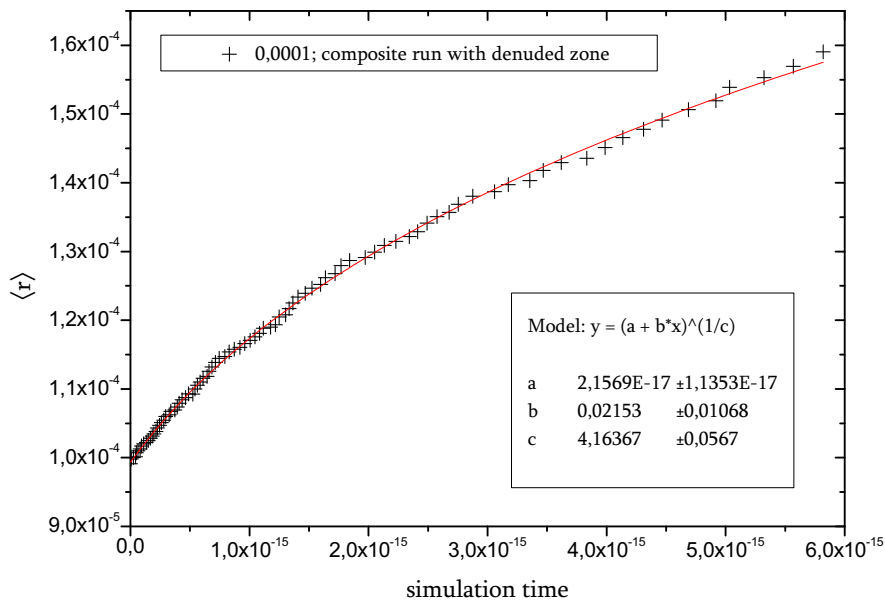


Figure 3.9: Time evolution of the mean island radius for the initial areal coverage $\Theta = 0,0001$ with initial denuded zone (crosses; from composite run with $k = 2$) and fit of these data by (3.2) (solid red line).

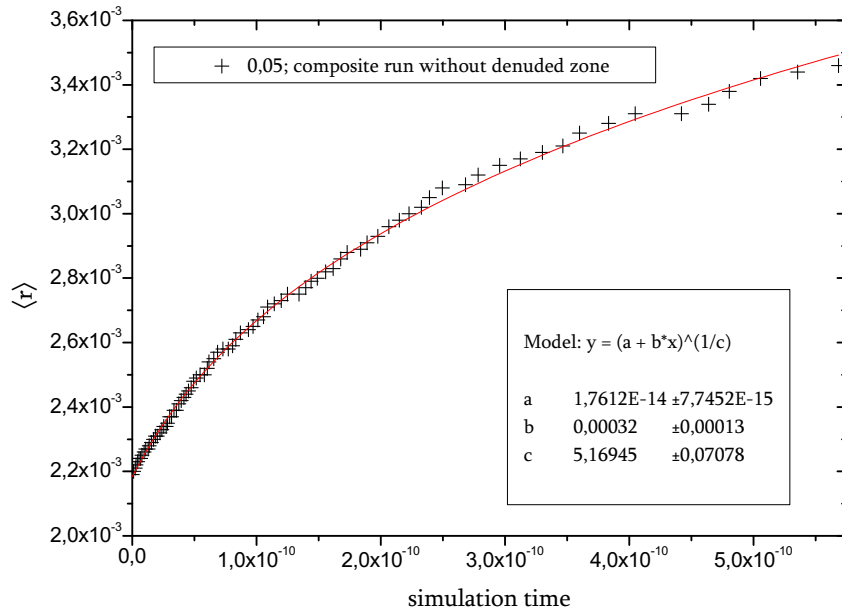


Figure 3.10: Time evolution of the mean island radius for the initial areal coverage $\Theta = 0,05$ without initial denuded zone (crosses; from composite run with $k = 2$) and fit of these data by (3.2) (solid red line).

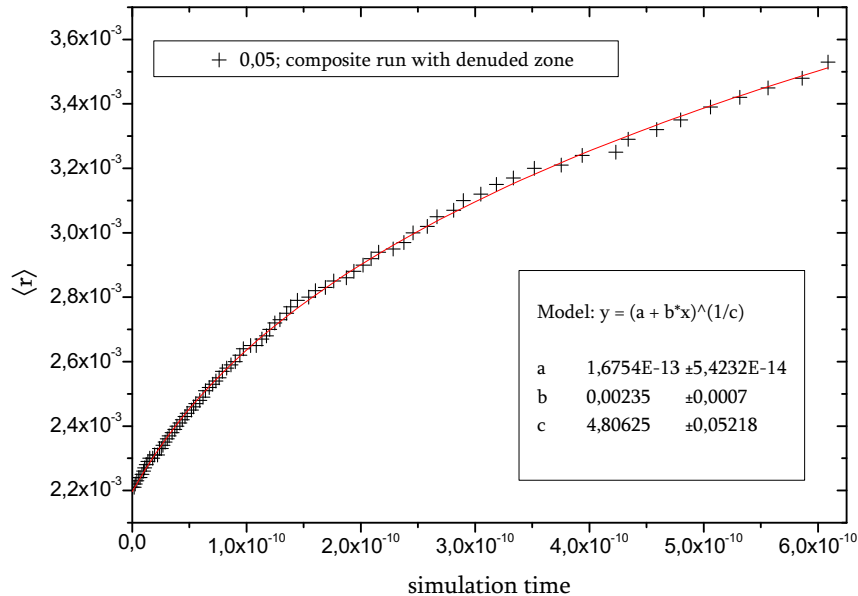


Figure 3.11: Time evolution of the mean island radius for the initial areal coverage $\Theta = 0,05$ with initial denuded zone (crosses; from composite run with $k = 2$) and fit of these data by (3.2) (solid red line).

3.2 Shape histograms

The distribution of island radii found in our simulation is apparently different from the one predicted by the LSW theory. The simulated distribution function is less sharply peaked and wider; it is also more symmetric. The height of the maximum decreases with increasing initial coverage (see figure 3.12) which is expected since the greater the coverage, the stronger the interactions.

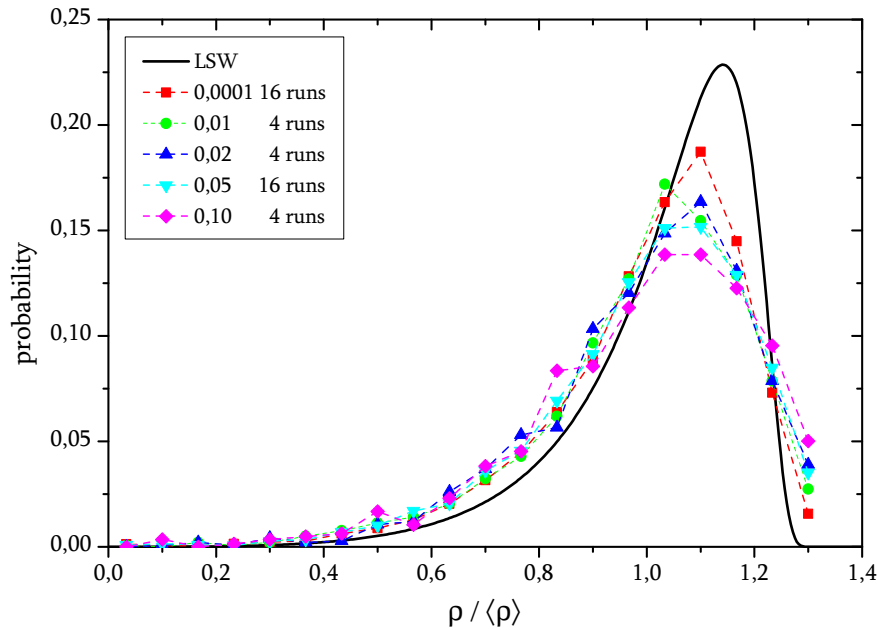


Figure 3.12: The distribution of island radii scaled with respect to the mean island radius for various areal coverages: $\Theta = 0,0001$ (red squares), averaged from 16 runs; $\Theta = 0,01$ (green circles), averaged from 4 runs; $\Theta = 0,02$ (dark blue triangles), averaged from 4 runs; $\Theta = 0,05$ (light blue triangles), averaged from 16 runs; and $\Theta = 0,10$ (violet diamonds), averaged from 4 runs. The LSW distribution is plotted for comparison (solid black line).

The distribution function seems to be dependent on whether the denuded zone has been used to generate the initial population of islands or not. Simulations with denuded zone show a slightly more pronounced peak; this observation is valid both for $\Theta = 0,0001$ and $\Theta = 0,05$ as can be seen from figures 3.13 and 3.14. Since the long-time behavior should be independent of the initial conditions, we can conclude that at the end of our simple runs the system has not yet reached the asymptotic regime. The distribution functions obtained from composite simulation runs should therefore be used, but, unfortunately, these do not provide reliable information due to insufficient statistics.

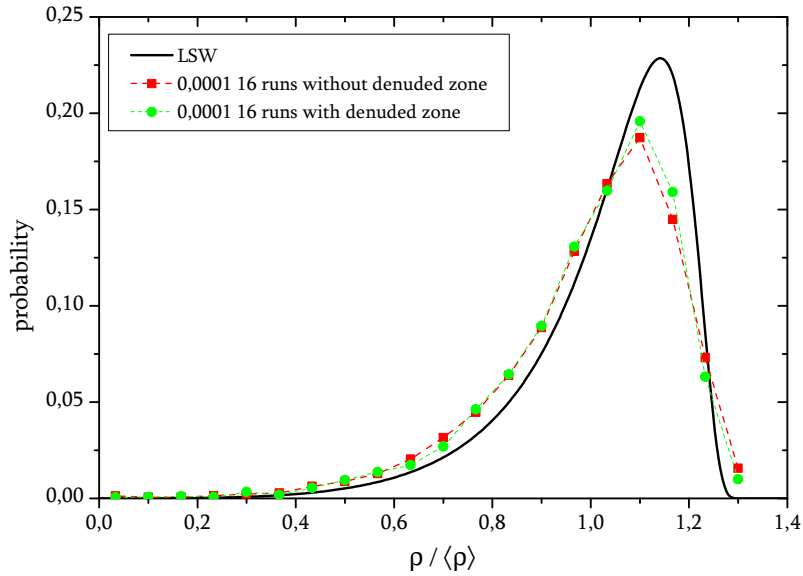


Figure 3.13: Comparison of the scaled island size distribution function for $\Theta = 0,000 1$ without the denuded zone (red squares) and with denuded zone ($\alpha = 2,50$; green circles). These distributions were obtained by averaging 16 simple runs in each case. The LSW function is plotted for comparison (solid black line).

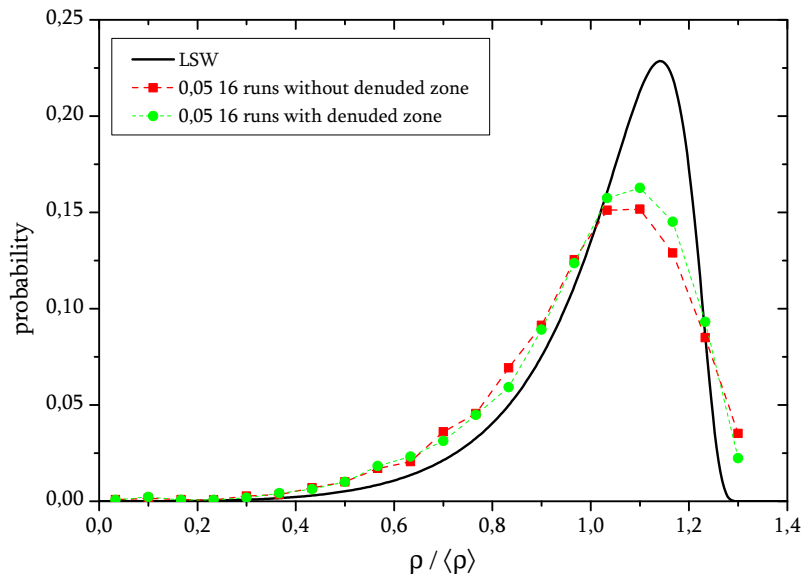


Figure 3.14: Comparison of the scaled island size distribution function for $\Theta = 0,05$ without the denuded zone (red squares) and with denuded zone ($\alpha = 50$; green circles). These distributions were obtained by averaging 16 simple runs in each case. The LSW function is plotted for comparison (solid black line).

We also compared the simulations with the distribution functions obtained from experiment (figure 3.15). In this experiment, gallium was deposited onto Si(100) surface with constant deposition flux of 1 ML/6 min at 300°C for 24, 96 and 194 minutes with the resulting Ga areal coverages of 0,15 in the first two cases and 0,20 in the third case. After the deposition, flat Ga islands (several hundreds of nanometers wide and less that 100 nm high) can be found on the surface. The island radii were measured *ex situ* by the atomic force microscopy (AFM). We can see that the experimental distributions are narrower and more symmetric than the ones obtained by experiment. This is caused by the effect of the nonzero deposition flux [4].

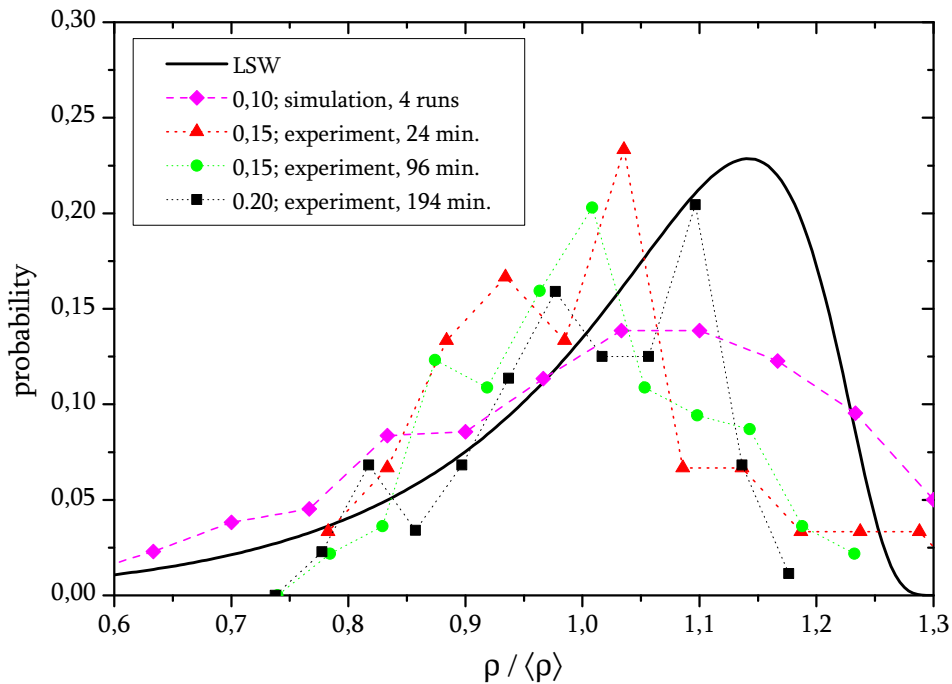


Figure 3.15: Comparison of the scaled island size distribution function predicted by the LSW theory (solid black line) with the distribution functions obtained from simulation for $\Theta = 0,10$ (violet diamonds) and from experiment with $\Theta = 0,15$ after 24 min. deposition (red triangles), $\Theta = 0,15$ after 96 min. deposition (green circles) and $\Theta = 0,20$ after 194 min. deposition (black squares). See the text for details.

3.3 Spatial histograms

As there is no theoretical prediction concerning the distribution of nearest neighbors, we concentrated only on the description of the data obtained from our simulations. We fitted the data using a gamma distribution [25] instead of Gaussian distribution [9] since (i) the Gaussian distribution is defined for arbitrary value of the independent variable whereas $r / \langle d_{nn} \rangle$ can attain only nonnegative values and (ii) the Gaussian function has zero skewness which is apparently not true for our data.

The gamma distribution is described by two parameters k and θ . In terms of these parameters all the important quantities could be calculated: the mean value is $k\theta$, the variance is $k\theta^2$ and the skewness is $2k^{-1/2}$. The results of the fits are summarized in tables 3.2 and 3.3. Note that the mean value should be equal to unity if the nearest-neighbor distribution was given by a gamma distribution since the data are normalized with respect to the mean nearest-neighbor distance; in all cases the mean values are indeed equal to unity within the standard deviation. The results clearly show that with increasing coverage, the distributions are more sharply peaked and more symmetric.

Θ	k	θ	$k\theta$	$\sqrt{k\theta^2}$	$2k^{-1/2}$
0,000 1	$5,1 \pm 0,2$	$0,205 \pm 0,009$	$1,04 \pm 0,06$	$0,46 \pm 0,02$	$0,89 \pm 0,02$
0,01	$6,7 \pm 0,4$	$0,15 \pm 0,01$	$1,01 \pm 0,09$	$0,39 \pm 0,03$	$0,77 \pm 0,02$
0,02	$7,2 \pm 0,5$	$0,14 \pm 0,01$	$1,0 \pm 0,1$	$0,38 \pm 0,04$	$0,74 \pm 0,03$
0,05	$9,6 \pm 0,1$	$0,105 0 \pm 0,000 1$	$1,01 \pm 0,01$	$0,325 \pm 0,002$	$0,645 \pm 0,004$
0,10	$12,2 \pm 0,7$	$0,083 \pm 0,005$	$1,01 \pm 0,08$	$0,29 \pm 0,02$	$0,57 \pm 0,02$

Table 3.2: Parameters of the gamma distribution used to fit the simulation results for various initial areal coverages obtained from simulations without the initial denuded zone.

Θ	k	θ	$k\theta$	$\sqrt{k\theta^2}$	$2k^{-1/2}$
0,000 1N	$5,1 \pm 0,2$	$0,205 \pm 0,009$	$1,04 \pm 0,06$	$0,46 \pm 0,02$	$0,89 \pm 0,02$
0,000 1D	$6,7 \pm 0,4$	$0,15 \pm 0,01$	$1,02 \pm 0,09$	$0,39 \pm 0,03$	$0,77 \pm 0,02$
0,05N	$9,6 \pm 0,1$	$0,105 0 \pm 0,000 1$	$1,01 \pm 0,01$	$0,325 \pm 0,002$	$0,645 \pm 0,004$
0,05D	13 ± 1	$0,074 \pm 0,006$	$1,0 \pm 0,1$	$0,27 \pm 0,02$	$0,55 \pm 0,02$

Table 3.3: Parameters of the gamma distribution used to fit the simulation results for initial areal coverages $\Theta = 0,001$ and $\Theta = 0,05$ with denuded zones (labeled with D) and without the denuded zones (N).

The comparison of the nearest-neighbor distributions for various coverages is complicated by the fact that these curves *have* to be different: because an island has nonzero radius, there are no other islands closer than ρ which results in the fact that the distribution function is shifted to larger values of $r/\langle d_{nn} \rangle$. Since for larger areal coverages the islands are bigger, this shift should increase with increasing Θ , which is indeed observed (see figure 3.16). On the other hand, for larger coverages there is less space on the surface which reduces the probability of finding large nearest-neighbor separations. This explains the fact that the width of the distribution decreases with increasing Θ .

The same effect as described in the previous paragraph is observed when we compare results for the same coverage, but with and without the denuded zone. This is not surprising because when placing islands, (i) their effective radius is bigger and (ii) the effective areal coverage is larger. This can be seen in figs. 3.17 and 3.18.

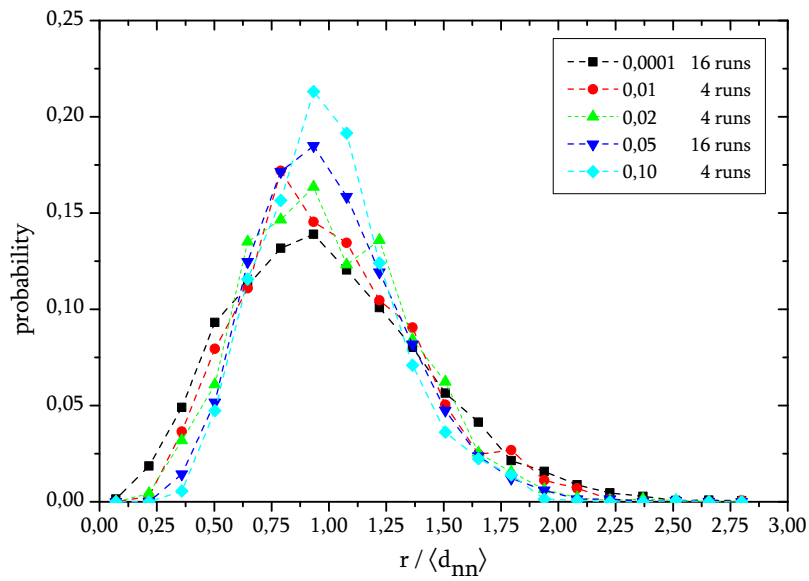


Figure 3.16: Comparison of the scaled nearest-neighbor distribution function for various initial areal coverages: $\Theta = 0,0001$ (black squares, from 16 runs), $\Theta = 0,01$ (red circles, 4 runs), $\Theta = 0,02$ (green triangles, 4 runs), $\Theta = 0,05$ (dark blue triangles, 16 runs) and $\Theta = 0,10$ (light blue diamonds, 4 runs). All the initial data sets were generated without the denuded zones.

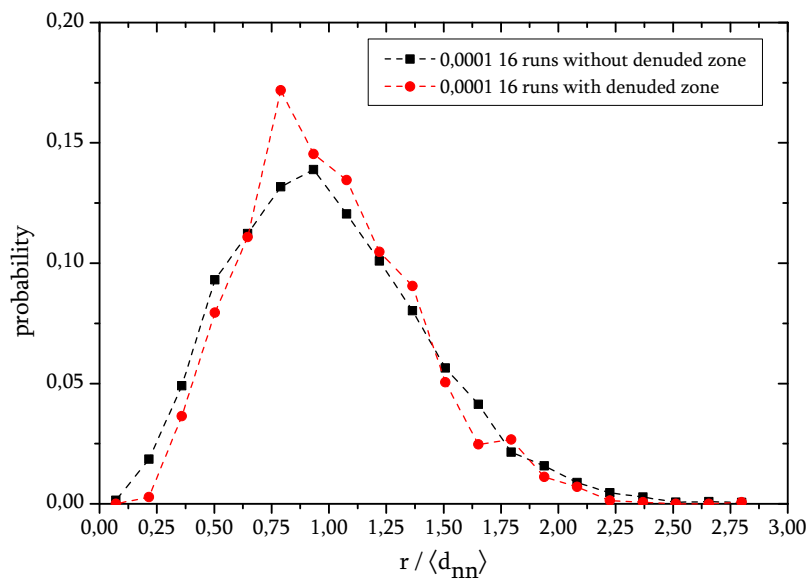


Figure 3.17: Comparison of the scaled nearest-neighbor distribution function for $\Theta = 0,0001$ without the denuded zone (black squares) and with denuded zone (red circles). The curves were obtained by averaging data from 16 single runs in both cases.

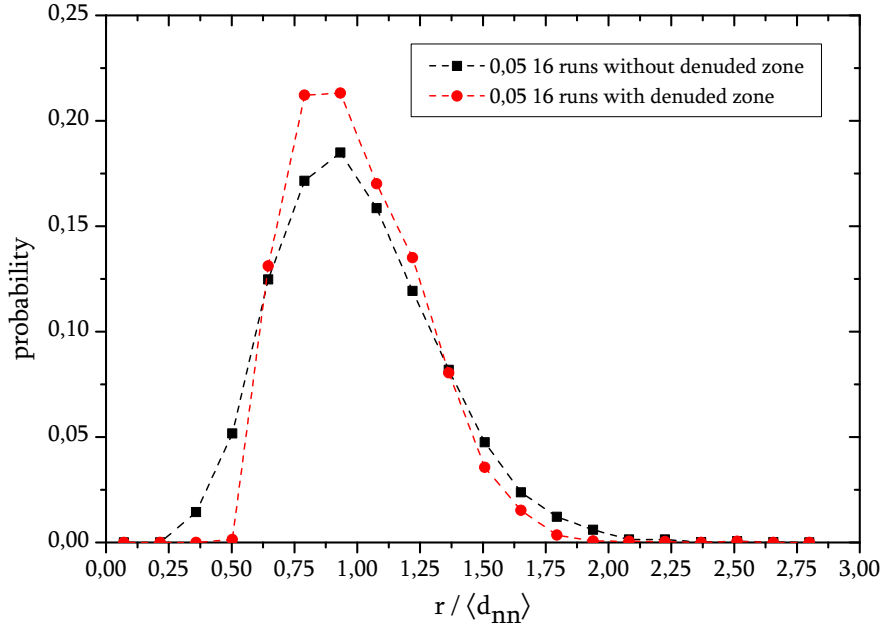


Figure 3.18: Comparison of the scaled nearest-neighbor distribution function for $\Theta = 0,05$ without the denuded zone (black squares) and with denuded zone (red circles). The curves were obtained by averaging data from 16 single runs in both cases.

3.4 Radial distribution functions

Radial distribution functions (RDF's), defined in section 1.3, provide us with important information on the denuded zones around the islands. The RFD's were evaluated in the following manner: we took the computation cell at the end of the simulation, created a total of nine identical copies and assembled them into a large 3×3 cell. This was necessary to avoid problems with particles close to the edge of the original cell. Then we took one island in the central subcell and sorted the other islands according to their distance. This was repeated for each island in the central subcell and the results were averaged. In the next step, we scaled the distances with respect to the mean nearest-neighbor distance. Finally, we calculated the expected number of particles in a shell of radius r from the island number density ($\mathcal{N} = 1/N$ since $L = 1$ in our simulations). From this the RDF was estimated using the definition (1.9). The results for various initial areal coverages are in figure 3.19 and the comparison of simulations with and without the denuded zone for two different coverages are in figures 3.20 and 3.21.

We found that even in simulations without initial denuded zones (fig. 3.19) these appear in the course of ripening. Two facts should be noted: first, there is always a certain region where the RDF is equal to zero since the islands have a nonzero radius; the extent of this region depends on the quotient of the mean island radius and the mean nearest-neighbor distance. This quotient is time-dependent which makes it hard to compare the results of simulations with different initial conditions. Second, the total

extent of the denuded zone seems to decrease with increasing coverage and varies from approximately $2 \times \langle d_{nn} \rangle$ for $\Theta = 0,0001$ to $1 \times \langle d_{nn} \rangle$ for $\Theta = 0,10$. This decrease was observed also in 3D/3D systems [8] and 2D/2D systems [16].

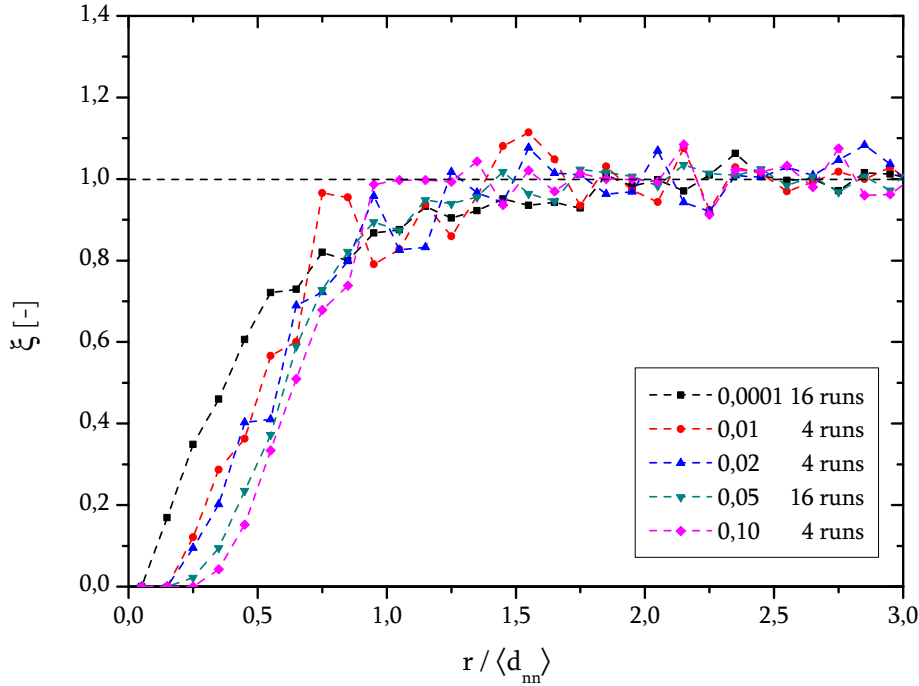


Figure 3.19: Comparison of the radial distribution functions for various initial areal coverages: $\Theta = 0,0001$ (black squares, from 16 runs), $\Theta = 0,01$ (red circles, 4 runs), $\Theta = 0,02$ (blue triangles, 4 runs), $\Theta = 0,05$ (green triangles, 16 runs) and $\Theta = 0,10$ (violet diamonds, 4 runs). All the initial data sets were generated without the denuded zones.

The RDF look quite differently if the initial denuded zones are present. However, the total extent of the denuded zone at the end of the simulation is again $\approx 1,5 \times \langle d_{nn} \rangle$. There is one more interesting thing: the initial denuded zones begin to be filled; the RDF is small but nonzero for small values of $r / \langle d_{nn} \rangle$ at the end of the simulation whereas it was exactly zero at the beginning for the same values. In the asymptotic RDF's obtained from composite runs (figs. 3.22 and 3.23) the difference between the simulations with and without the initial denuded zone has disappeared; however, the extent of the denuded zone cannot be estimated due to missing statistics.

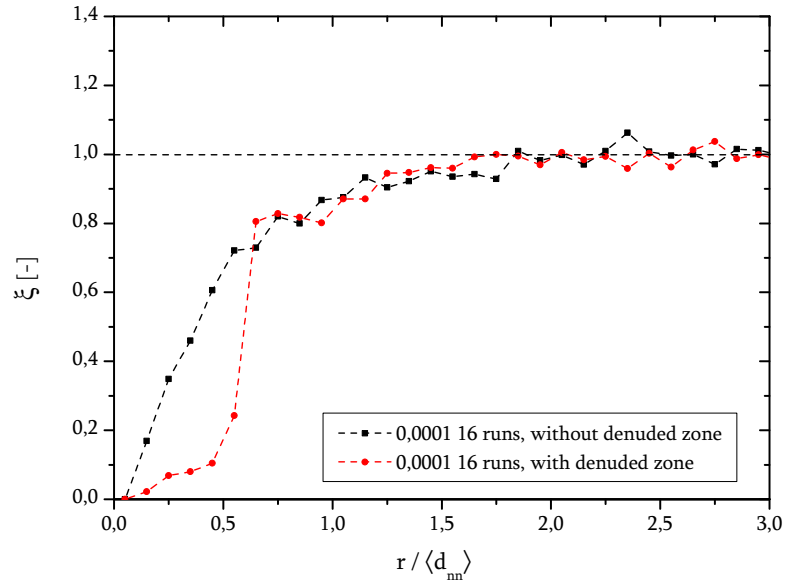


Figure 3.20: Comparison of the RDF for $\Theta = 0,0001$ without the initial denuded zone (black squares) and with initial denuded zone (red circles). The curves were obtained by averaging data from 16 single runs in both cases.

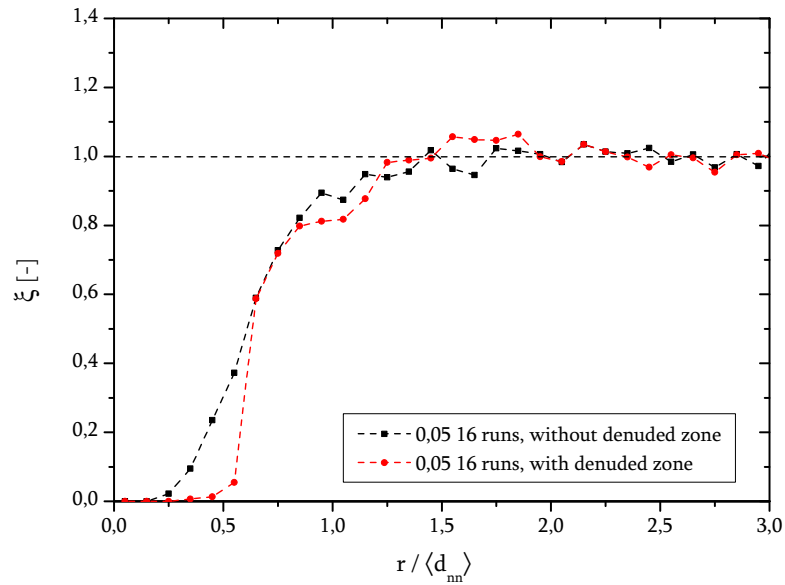


Figure 3.21: Comparison of the RDF for $\Theta = 0,05$ without the initial denuded zone (black squares) and with initial denuded zone (red circles). The curves were obtained by averaging data from 16 single runs in both cases.

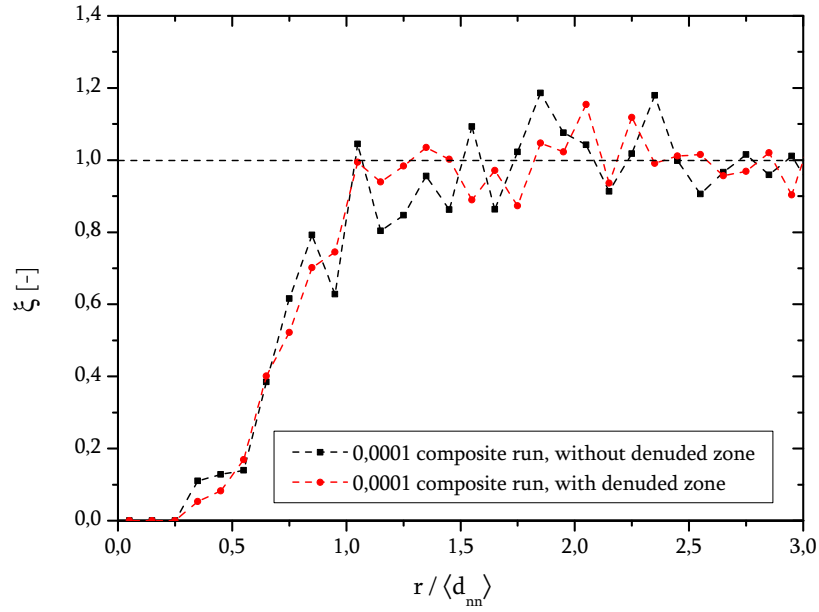


Figure 3.22: Comparison of the RDF for $\Theta = 0,000\ 1$ without the initial denuded zone (black squares) and with initial denuded zone (red circles). The curves were obtained from composite runs with $k = 2$ in both cases.

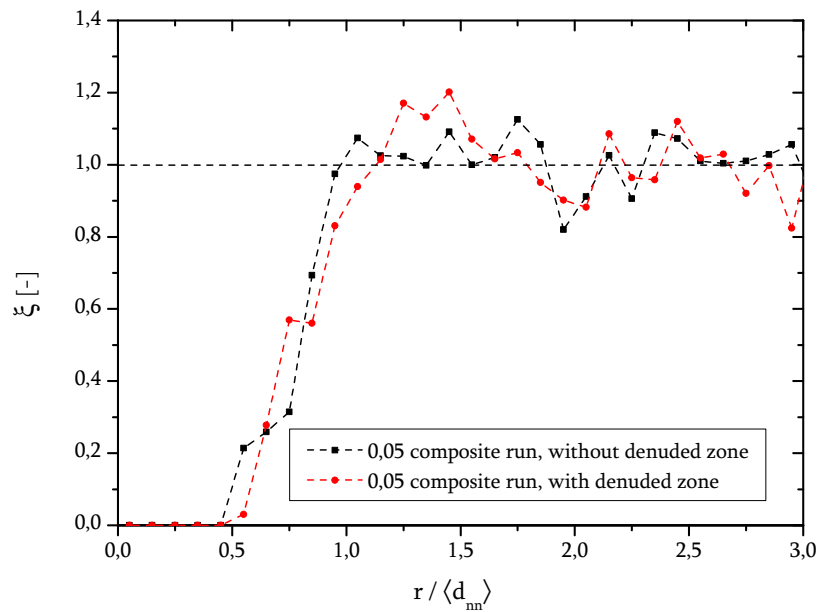


Figure 3.23: Comparison of the RDF for $\Theta = 0,05$ without the initial denuded zone (black squares) and with initial denuded zone (red circles). The curves were obtained from composite runs with $k = 2$ in both cases.

Conclusion

Overview of the simulation results

The LSW theory predicts that the mean island radius scales with time as $\langle \rho \rangle \sim t^{1/4}$ for t large enough. However, this prediction is valid only if the growth constant does not depend on time, which is not true. According to [4] the power-law scaling is then valid only for short time intervals. We hoped that the deviation from the power-law scaling would be small enough for our results to be comparable with the LSW theory. We fitted the simulated data by a function of the form predicted by the LSW theory and we obtained scaling exponents between 3,13 and 5,17 with no apparent dependence on the simulation conditions while the other fitting parameters were in strong disagreement with the values obtained from the fit. We can therefore conclude that the power-law scaling of the mean island radius predicted by the LSW theory is not valid. More recent studies predict that the mean island radius grows roughly as $(t/\ln t)^{1/3}$ and that there is no scaling at all [4].

We have compared the distribution functions of the island radii with the LSW prediction to find that the simulated distributions are broader and more symmetric with the broadening being more pronounced for larger initial areal coverages. This is consistent with both the theoretical prediction and experimental results [4].

Spatial correlations were studied using the nearest-neighbor distance distribution function and the radial distribution function. Unfortunately, there are no analytical results and very few experimental studies or simulations available at this time. The nearest-neighbor distance distribution was examined in an experimental study of ripening of Sn clusters on Si(111) surface [9]. The measured distributions were fitted by a Gaussian distribution and the scaled standard deviations $\sigma/\langle d_{nn} \rangle$ were found to be close to $0,21 \pm 0,02$ in most cases. We used a gamma distribution to fit our data since the Gaussian distribution cannot in principle be used because $r/\langle d_{nn} \rangle$ attains only positive values. We found that in simulations without initial denuded zones the standard deviation decreases from $0,46 \pm 0,02$ to $0,29 \pm 0,02$ with the initial areal coverage decreasing from 0,0001 to 0,10. If we compare the simulations with and without the denuded zone for the same areal coverage we find that the distribution is broader in the latter case. It should also be noted that in the distributions obtained from simulations without the denuded zone memory effects of initial random island placement are clearly distinguishable whereas the distributions with initial denuded zones are similar to the experimental results [9].

When analyzing the radial distribution functions we found that there is a denuded zone around each island whose extent (measured with respect to the mean nearest-neighbor distance) increases with decreasing areal coverage. We compared simulations in which the islands were placed with the initial denuded zone with simulations where there is initially no such zone to find that at the end of the simulation the size of the denuded zone is approximately the same in both cases. Both experimental and

computational studies show that the radial distribution grows from zero value until it reaches a local maximum with $\xi > 1$; this maximum is followed by a slow decline to the asymptotic value $\xi = 1$. Such local maxima were not observed in our results because the height of the maximum increases with increasing coverage [4, 8, 16, 6] and for the areal coverages used in our study it cannot be distinguished from fluctuations present due to insufficient statistics.

Possible extensions of the model

The monopolar approximation employed in the model is valid when the areal coverage is lesser than approximately 0,10 [8, 16]. For larger areal coverages it is necessary to use higher-order approximations. These approximations not only allow for higher areal coverages but they bring entirely new qualitative features to the model. In the *dipolar approximation*, the islands are mobile, with the dipole terms being directly related to the velocity of the centre of mass of the islands [16]. It is also possible to relieve the constraint of fixed island shape in 2D/2D systems [6] but the applicability to 3D/2D remains an open issue.

The problem of diverging concentration fields inherent to steady-state diffusion equation in two dimensions is resolved due to the mass conservation condition (or the screening-length concept, which is based on this condition). However, the restriction to mass-conserved systems is very inconvenient and there were attempts to relieve this restriction. Rogers and Desai [26] attempted to use the non-steady state diffusion equation but at the cost of major simplification including a mean-field approximation while Hayakawa and Family used perturbation theory to solve the many-body diffusion problem [27].

The ripening is usually considered to be driven by capillarity effect which is expressed by the Gibbs-Thomson boundary condition. More recently, the importance of elastic strain has been recognised [28, 29]. These effect can be taken into account by replacing the Gibbs-Thomson condition; a very simple example of how this can be done is shown in [14].

Applicability of the LSW theory

The main purpose of this work was to determine whether the simple LSW mean-field theory can at least roughly describe the Ostwald ripening process in mixed 3D/2D system. Based on the discussion in section 3.4 it is obvious that the Chakraverty's extension [12] of the LSW theory to 3D/2D systems is unsatisfactory and that its use should be avoided. This is rather inconvenient because there is no other model of such simplicity.

In addition, we have shown that the extrapolation of the 3D/3D and 2D/2D models from [7] to 3D/2D can be used to describe ripening in the mixed-dimensional case as the principal features are in agreement with the results of other groups, either experimental studies or simulations. Although this model can be extended to be applicable to cases with very large areal coverages and perhaps to include elastic strain effects, its validity remains limited to mass-conserved systems.

Bibliography

- [1] K. Oura, V. G. Lifshits, A. A. Saranin, A. V. Zotov and M. Katayama, *Surface Science: An Introduction*, Berlin, Heidelberg: Springer-Verlag, 2003. ISBN 3-540-00545-5.
- [2] A. Lo and R. T. Skodje, *J. Chem. Phys.* **112** (2000), 1 966.
- [3] T. R. Mattsson, G. Mills and H. Metiu, *J. Chem. Phys.* **110** (1999), 12 151.
- [4] M. Zinke-Allmang, *Thin Solid Films* **346** (1999), 1.
- [5] H. Xia and M. Zinke-Allmang, *Physica A* **261** (1998), 176.
- [6] N. Akaiwa and D. I. Meiron, *Phys. Rev. E* **54** (1996), R13.
- [7] J. H. Yao, K. R. Elder, H. Guo and M. Grant, *Phys. Rev. B* **47** (1993), 14 110.
- [8] N. Akaiwa and P. W. Voorhees, *Phys. Rev. E* **49** (1994), 3 860.
- [9] G. R. Carlow and M. Zinke-Allmang, *Phys. Rev. Lett.* **78** (1997), 4 601.
- [10] I. M. Lifshitz and V. V. Slyozov, *J. Phys. Chem. Solids* **19** (1961), 35.
- [11] C. Wagner, *Z. Elektrochem.* **65** (1961), 581.
- [12] B. K. Chakraverty, *J. Phys. Chem. Solids* **28** (1967), 2 401.
- [13] J. A. Marqusee, *J. Phys. Chem* **81** (1984), 976.
- [14] M. Iwamatsu and Y. Okabe, *J. Appl. Phys.* **86** (1999), 5 541.
- [15] M. Zinke-Allmang, L. C. Feldman and S. Nakahara, *Appl. Phys. Lett.* **51** (1987), 975.
- [16] N. Akaiwa and D. I. Meiron, *Phys. Rev. E* **51** (1995), 5 408.
- [17] *Numerical Recipes in Fortran 77: The Art of Scientific Computing*, Cambridge: Cambridge University Press, 1992. ISBN 0-521-43064-X.
- [18] *Linear Algebra Package* [online]. v3.1.1., February 26, 2007 [cited May 16, 2008] (<http://www.netlib.org/lapack/>).
- [19] *Basic Linear Algebra Subroutines* [online]. Last updated May 2, 2008 [cited May 16, 2008] (<http://www.netlib.org/blas/>).

- [20] *AMD Math Core Library* [online]. Last updated May 16, 2008 [cited May 16, 2008] [⟨http://developer.amd.com/cpu/libraries/acml/Pages/default.aspx⟩](http://developer.amd.com/cpu/libraries/acml/Pages/default.aspx).
- [21] *Intel Math Kernel Library* [online]. Last updated May 16, 2008 [cited May 16, 2008] [⟨http://www.intel.com/cd/software/products/asm-na/eng/345631.htm⟩](http://www.intel.com/cd/software/products/asm-na/eng/345631.htm).
- [22] *Intel Visual Fortran compiler* [online]. Version 10.1.029 [downloaded March 19, 2008] [⟨http://www.intel.com/cd/software/products/asm-na/eng/278834.htm⟩](http://www.intel.com/cd/software/products/asm-na/eng/278834.htm).
- [23] *G95 Fortran compiler* [online]. Version 0.9 [downloaded November 5, 2007] [⟨http://www.g95.org/⟩](http://www.g95.org/).
- [24] *Numerical Recipes in Fortran 90: The Art of Parallel Scientific Computing*, Cambridge: Cambridge University Press, 1996. ISBN 0-521-57439-0.
- [25] *Gamma Distribution* [online]. Last updated May 12, 2008 [cited May 16, 2008] [⟨http://en.wikipedia.org/wiki/Gamma_distribution#Related_distributions⟩](http://en.wikipedia.org/wiki/Gamma_distribution#Related_distributions).
- [26] T. M. Rogers and R. C. Desai, Phys. Rev. B **3** (1989), 11 956.
- [27] H. Hayakawa and F. Family, Physica A **163** (1990), 491.
- [28] J. A. Floro, M. B. Sinclair, E. Chason, L. B. Freund, R. D. Twisten, R. Q. Hwang and G. A. Lucadamo, Phys. Rev. Lett. **84** (2000), 701.
- [29] A. V. Osipov, S. A. Kukushkin, F. Schmitt and P. Hess, Phys. Rev. B **64** (2001) 205 421.

Seznam příloh

1. Program `Deposit` pro generování počáteční populace ostrůvků (ver. 1.01), přiloženo na CD, `BP/0sSim 1.13/Deposit.exe`.
2. Program `0sSim` pro simulaci časového vývoje populace ostrůvků (ver. 1.13), přiloženo na CD, `BP/0sSim 1.13/0sSim.exe`.
3. Zdrojový kód k programům `Deposit` a `0sSim` spolu se zdrojovým kódem k rutinám z knihovny BLAS [19] a rutině DSYSV z knihovny LAPACK [18], přiloženo na CD, `BP/0sSim 1.13/0sSim.v1.13.Source.Code.zip`.
4. Zdrojové soubory pro zpracování simulovaných dat v programu Matlab (ver. 7.1); přiloženo na CD ve složce `BP/Matlab/`.

POPISNÝ SOUBOR ZÁVĚREČNÉ PRÁCE

Autor: Bc. Tomáš Čechal

Název závěrečné práce: Ostwaldovo zrání – teoretický popis a simulace.

Název závěrečné práce ENG: Ostwald ripening – theoretical description and simulation.

Anotace závěrečné práce: Tato práce se zabývá popisem Ostwaldova zrání trojrozměrných ostrůvků deponovaných na rovinných površích. V první kapitole jsou představeny dvě teorie Ostwaldova zrání: LSW teorie založená na aproximaci středního pole a mnohačasticová teorie vycházející z řešení difuzní rovnice v kvazistatické aproximaci. Ve druhé kapitole je popsán algoritmus numerického řešení rovnic získaných z mnohačasticové teorie. Výsledky numerického řešení jsou ve třetí kapitole srovnány s předpověďmi LSW modelu.

Bylo zjištěno, že předpovědi standardní LSW teorie popisující systémy s dvourozměrným transportem hmoty jsou v ostrém protikladu jak s výsledky získanými z dokonalejšího mnohačasticového modelu, tak s experimenty popsány v uvedených pramenech. Mnohačasticový model založený na difuzní rovnici poskytuje výsledky konzistentní s jinými teoriemi i experimentem.

Anotace závěrečné práce ENG: This thesis deals with Ostwald ripening of three-dimensional clusters deposited on a two-dimensional surface. In the first chapter two distinct theories of Ostwald ripening are presented: the mean-field LSW theory and a many-body theory based on the solution of the diffusion equation in quasistationary approximation. In second chapter the algorithm used for numerical solution of the equations obtained from the many-body theory is described. The results extracted from the numerical solution are compared with predictions of the LSW model in the third chapter.

POPISNÝ SOUBOR ZÁVĚREČNÉ PRÁCE

We found that the standard LSW theory of systems with two-dimensional mass transport should not be used in practice because its predictions are in strong disagreement with the results obtained both from the more elaborate diffusion-equation model and from experimental studies described in references. On the other hand, the diffusion equation based model gives results consistent with other theories and experiments.

Klíčová slova: fázová separace, Ostwaldovo zrání, LSW teorie, numerická simulace

Klíčová slova ENG: phase separation, Ostwald ripening, LSW theory, numeric simulation

Typ závěrečné práce: bakalářská práce

Datový formát elektronické verze: pdf

Jazyk závěrečné práce: angličtina

Přidělovaný titul: Bc.

Vedoucí závěrečné práce: Ing. Jan Čechal, Ph.D.

Škola: Vysoké učení technické v Brně

Fakulta: Fakulta strojního inženýrství

Ústav / ateliér: Ústav fyzikálního inženýrství

Studijní program: Aplikované vědy v inženýrství

Studijní obor: Fyzikální inženýrství